Detecting Microstructures in Magnetic Resonance Imaging with a Spin-lock Pulse Sequence

Alexandra van Dongen

Mars Lab TU Delft

Detecting Microstructures in Magnetic Resonance Imaging with a Spin-lock Pulse Sequence

by

Alexandra van Dongen

to obtain the degree of Master of Science in Biomedical Engineering,
track Medical Devices,
at the Delft University of Technology,
to be defended publicly on Thursday February 27, 2025 at 15:45.

Student number:	4885570	
Project duration:	May 23, 2024 – Feb 27, 2025	
Thesis committee:	Dr. S.D. Weingärtner,	TU Delft, main supervisor
	Prof. dr. ir. P. Breedveld,	TU Delft
	MSc. A. Arami,	TU Delft, daily supervisor

Cover image from Adobe Stock.

Abstract

Elevated micrometer-scale iron deposits in the brain are a crucial early detection marker for numerous neurodegenerative diseases. Although iron deposits exist below conventional magnetic resonance imaging resolution, sub-voxel information on their spatial properties can be encoded into the MR signal through magnetic susceptibility differences and diffusion effects. Spin-lock pulse sequences have recently emerged as a powerful tool sensitive to diffusion-mediated dephasing, characterized by the time constant $T_{1\rho}$. By employing continuous low-frequency radiofrequency pulses, signal dynamics can be sensitized to motions in the order of sub-kilohertz, rendering it sensitive to the effect of diffusion. In this work, the potential of microstructure characterization with $T_{1\rho}$ was explored through simulation and phantom experiments. A Monte Carlo simulation of a conventional spin-lock pulse showed high sensitivity to microbead radius, concentration, and susceptibility shift through $R_{1\rho}$ dispersion magnitude and inflection point. Phantom experiments of a balanced and refocused spin-lock pulse demonstrated minimal changes in relaxation rate, suggesting that a considerable susceptibility gradient must be present before signal dynamics are affected. By overcoming current experimental limitations, spin-lock pulse sequences hold great promise as reliable tools for probing structures of micrometer size.

Abbreviations

Abbreviation	Definition
ADC	Apparent diffusion coefficient
B	Magnetic field
BOLD	Blood oxygenation level-dependent imaging
$CuSo_4$	Copper sulfate
D	Diffusion coefficient
dHB	Deoxyhemoglobin content
DWI	Diffusion weighted imaging
dTE	Delta echo time
EPI	Echo-planar imaging
FFE	Fast field (gradient) echo
FOV	Field of view
f_{SL}	Spin-lock frequency
Gd	Gadolinium
GraSE	Gradient and spin echo
$HoCl_3.6H_20$	Holmium chloride hexahydrate
M	Net magnetization
MC	Monte Carlo
MR	Magnetic resonance
MRI	Magnetic resonance imaging
NH_2	Amine group
$NiCl_2$	Nickel chloride
PA	Polyacrylamide
PEG	Polyethylene glycol
RF	Radiofrequency
ROI	Region of interest
SAR	Specific absorption rate
SE	Spin echo
SL	Spin-lock
T_1 & R_1	Longitudinal relaxation time & rate
T_2 & R_2	Transverse relaxation time & rate
T_2^* & R_2^*	Observed transverse relaxation time & rate
$T_{1\rho}$ & $R_{1\rho}$	Longitudinal relaxation time & rate in the rotating frame of reference
TE	Echo time
TFE	Turbo field (gradient) echo
TR	Repetition time
t_{SL}	Spin-lock time
VSI	Vessel size imaging

Contents

1

Introduction

Microstructures provide valuable information on tissue states, enabling early detection and disease monitoring of pathologies as neurodegenerative diseases. Specifically, elevated micrometer-scale iron deposits in the brain are associated with Alzheimer's disease, Parkinson's disease, and dementia [1]. Although iron is essential for cell function, increased levels cause oxidative damage to brain tissue. Detecting and quantifying these microstructural changes non-invasively and timely provides a means to improve early diagnosis, monitor disease progression, and evaluate treatment efficacy. However, the spatial scale of microstructures poses significant diagnostic difficulties in non-invasive detection.

MRI as non-invasive tool has gained interest for microstructure detection despite its relatively large resolution. *In vivo* microstructures such as iron deposits [1, 2], lung alveoli [3], labeled cells [4], and regions with exogenous contrast agents [5] affect signal dynamics, thereby encoding spatial information below the resolution limit into the image. The signal is affected by small magnetic field inhomogeneities generated around microstructures due to inherent magnetic susceptibility differences to the surrounding tissue. Additionally, the diffusion of hydrogen spins, which serve as our sensor in MR imaging, is non-negligible in the presence of field inhomogeneities. Understanding the relation between susceptibility variations and diffusion is essential for the precise quantification of microscopic magnetic tissue inhomogeneities. This sensitivity enables MRI to reveal tissue composition and pathology, even at micrometer size.

The transverse relaxation rate (R_2 and R_2^*) is highly sensitive to magnetic field inhomogeneities and diffusion - key aspects for microstructure detection. Therefore, many studies focus on T_2 and T_2^* relaxation to detect magnetic perturbers of micrometer scale [6–9]. The theoretical formalisms of susceptibility and diffusion effects on transverse relaxation are well understood, stating that static and dynamic dephasing are the primary contributors to signal dynamics [10]. In this regard, techniques such as blood oxygenation level-dependent imaging (BOLD) and vessel size imaging (VSI) have been studied extensively. BOLD imaging depends on the deoxyhemoglobin (dHb) content. Due to its intrinsic susceptibility, the presence of dHb increases the transverse relaxation rate, providing additional image contrast [11]. In VSI, an intravascular superparamagnetic contrast agent causes changes in R_2 and R_2^*, where the ratio $\Delta R_2/\Delta R_2^*$ is used to calculate a weighted mean of the vessel size [12].

Recently, $T_{1\rho}$ has gained interest as a needle-free and contrast agent-free technique that can visualize phenomena occurring at low interaction frequencies [13]. Unlike T_1 methods that probe molecular motions close to the Larmor frequency and T_2 and T_2^* methods that rely on transverse relaxation effects, $T_{1\rho}$ sensitizes the signal to motions similar to the effective precession frequency in the order of sub-kilohertz [14]. Hence, it holds great potential in shedding new light on the slow-motional process of spin diffusion [15].

$T_{1\rho}$ is characterized as spin-lattice relaxation in the rotating frame, which can be quantified with a spin-lock pulse sequence [16]. In such a sequence, magnetization is locked into the transverse plane with a continuous pulse at a certain spin-lock frequency, preventing normal free precession and spin dephasing. $T_{1\rho}$ is sensitive to both diffusion and chemical exchange processes, while these processes can be distinguished based on their time scales [15]. With faster time scales, a basis is provided to estimate chemical exchange rates [17, 18], while the mechanism of diffusion may be studied using lower interactional frequencies [14].

Although theoretical formalisms explaining $T_{1\rho}$ behavior are lacking, the ability to probe spin diffusion through susceptibility gradients offers a unique possibility to detect microstructures [19]. While preliminary studies in *in vivo* rat models demonstrate the feasibility of $T_{1\rho}$ in detecting microvascular changes, further investigation is needed to establish its robustness and clarify the relationship between microstructure geometry and signal dynamics [20].

In this work, the sensitivity and reliability of a spin-lock pulse sequence was systematically evaluated for detecting microstructural features in MRI. The effect of microstructure size, concentration and magnitude of the susceptibility gradient was evaluated through simulations and phantom experiments.

2

Theoretical background

In this chapter, the theoretical principles of MRI necessary to understand the effects of microstructures on signal dynamics are discussed. First, the fundamental concept of nuclear magnetism and the process of relaxation are introduced, followed by how spin diffusion through intrinsic susceptibility gradients in microstructure environments sheds light on their spatial characteristics.

2.1. Nuclear magnetism

The signal in magnetic resonance imaging (MRI) relies on nuclear magnetism. The concept of nuclear magnetism describes the phenomenon that particles exposed to an externally applied magnetic field will become aligned and precess around it, properties that depend on the particle spin [21].

Spin is an intrinsic form of angular momentum that is quantum in nature [21]. The nucleus of a particle with a non-zero spin creates a magnetic dipole moment μ proportional to the spin angular momentum J in accordance with Eq. 2.1. They are related through the gyromagnetic ratio, γ, a constant specific to the atomic species and often expressed in MHz/Tesla [22].

$$\mu = \gamma J, \tag{2.1}$$

Hydrogen is the most used nucleus in MRI due to its high natural abundance in biological tissue and its strong interactions with external magnetic fields. Since hydrogen particles have a non-zero spin, they possess an intrinsic magnetic dipole moment that causes particles to behave like tiny bar magnets when exposed to an external magnetic field. Hence, an ensemble of spins induces a net magnetization in a tissue that can be exploited to generate image contrasts depending on tissue type.

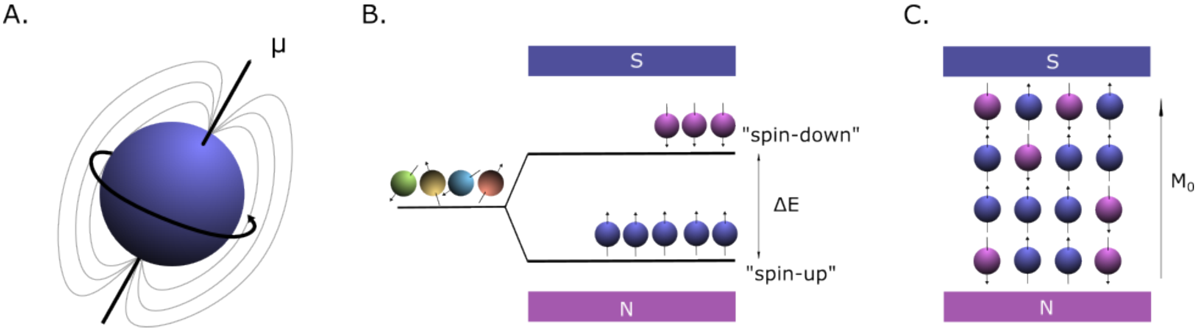

Figure 2.1: A) The magnetic moment μ of an atomic nucleus. B) The Zeeman splitting effect. When atomic nuclei are placed in an external magnetic field, they interact with it. In the case of a hydrogen atom, the nuclei will orient parallel or anti-parallel to the magnetic field, B_0. A potential energy gap ΔE arises between spin-up and spin-down states. C) A net magnetization forms as more spins align parallel to the field than antiparallel. Figure adapted from [23].

The net magnetization induced by an ensemble of particles with non-zero spin in a magnetic field occurs according to the Zeeman effect (Fig. 2.1). The Zeeman effect dictates that the intrinsic spin s of a particle determines its possible orientations in a magnetic field, given by $2s + 1$. A small potential energy gap between spin states, ΔE, arises following Eq. 2.2. Here, $\hbar$ is the reduced Planck constant, γ is the gyromagnetic ratio, and B_0 is the magnitude of the external magnetic field [23].

$$\Delta E = \frac{\mu}{s} B = \gamma \hbar B \tag{2.2}$$

A hydrogen spin with $s = 1/2$ has two spin states: parallel or antiparallel to the effective field. Spins will naturally distribute over the two spin states according to the principles of thermodynamics. The number of spins existing in a spin-up, N^+ and spin-down state, N^-, can be described using Boltzmann statistics as a function of ΔE, temperature T and the Boltzmann constant k [23]:

$$\frac{N^+}{N^-} = e^{-\frac{\Delta E}{kT}} \tag{2.3}$$

The combined effect of the spin-up and spin-down nuclei in a sample is known as the net magnetization, M. In MRI, the initial net magnetization M_0 is induced by a strong static magnetic field, B_0, that causes spins to exhibit the rotational motion of Larmor precession [24]. The Larmor frequency is the frequency at which the spins precess around the magnetic field, ω_0, and is dependent on the combined properties of the particle and of the static magnetic field (Eq. 2.4) [21] .

$$\omega_0 = \gamma B_0 \tag{2.4}$$

In thermal equilibrium, the magnetization precesses fully along the direction of the magnetic field, M_z. Lacking a time-varying transverse component, M_{xy}, no electrical current is induced in the receiver coil through electromagnetic induction. To induce a transverse magnetization, a rotating magnetic field B_1 is applied with a radiofrequency (RF) pulse tuned to match the Larmor frequency following the on-resonance principle [21]. To model the evolution of the magnetization vector in MRI, the Bloch equation can be used, which will be introduced in the following section.

2.2. Bloch equation

The Bloch equation classically describes the interactions of the magnetization vector M (M_x, M_y, M_z) with its surroundings through Larmor precession and relaxation (Eq. 2.5) [25]. Here, T_1 and T_2 indicate longitudinal and transverse relaxation times - the two most widely used causes of contrast in MRI. γ denotes the gyromagnetic ratio, $B(B_x, B_y, B_z)$ is the applied magnetic field, $\hat{x}, \hat{y}, \hat{z}$ are the unit vectors in the directions of the Cartesian coordinate system, and M_0 is the initial net magnetization. In the following section, the relaxation mechanisms will be described.

$$\frac{dM}{dt} = \gamma(M \times B) - \frac{M_x}{T_2}\hat{x} - \frac{M_y}{T_2}\hat{y} + \frac{M_0 - M_z}{T_1}\hat{z} \tag{2.5}$$

2.2.1. Relaxation

After the initial RF pulse, the net magnetization vector is no longer fully in the longitudinal plane, and a transverse magnetization M_{xy} is induced. The spin system will recover along the direction of the static magnetic field, M_z, by dissipating energy to the surrounding lattice until $M_z = M_0$. The rate of regrowth depends on the excess energy of the spin and a tissue-specific time constant, T_1, known as the longitudinal relaxation time. For time t after an RF pulse with flip angle α, M_z may be described as [23]:

$$\begin{aligned} M_z(t) &= M_0 \cdot cos(\alpha) + (M_0 - M_0 \cdot cos(\alpha)) \cdot (1 - e^{-\frac{t}{T_1}}), \\ M_z(t) &= M_0 \cdot (1 - e^{-\frac{t}{T_1}}) \quad \text{for} \quad \alpha = 90^\circ \end{aligned} \tag{2.6}$$

A frequently faster relaxation process is the loss of phase coherence due to spin-spin interactions. During the initial RF pulse, all magnetic moments precess in phase at the same frequency creating a magnetization in the transverse plane, M_{xy}. When the RF pulse is no longer applied, the magnetic moments fan out. The magnetic moment of one spin affects the observed magnetic field of a neighboring spin, leading to phase decoherence and a return to thermal equilibrium of $M_{xy} = 0$. The rate at which this occurs depends on the tissue-specific time constant, T_2. T_2 can only be measured directly by compensating for temporally invariant factors, such as static field inhomogeneities and magnetic susceptibility differences. Otherwise, spin-dephasing is caused by the combined effects of the true spin-spin relaxation (T_2) and spatial disparities in magnetic field strength (T_2'), which is characterized as T_2^* [23]:

$$\frac{1}{T_2^*} = \frac{1}{T_2'} + \frac{1}{T_2} \tag{2.7}$$

The detectable magnetization M_{xy} at time t following a flip-angle of 90° can be described by Eq. 2.8, where ω_0 denotes the Larmor frequency [23]:

$$M_{xy}(t) = \begin{pmatrix} cos(\omega_0 t) \\ sin(\omega_0 t) \\ 0 \end{pmatrix} M_0 \cdot e^{-\frac{t}{T_2^*}} \tag{2.8}$$

An alternative type of relaxation, not captured in Eq. 2.5, is the spin-lattice relaxation in the rotating frame of reference, $T_{1\rho}$. $T_{1\rho}$ is a fundamentally different relaxation process than T_1 and T_2. This type of relaxation occurs when the spin is locked in the rotating frame with a continuous resonant RF pulse (Fig. 2.5) [15, 26]. Under the spin-lock (SL) pulse, slow-motion frequencies similar to the effective precession frequency (ω_{eff}) are enhanced. The effective precession frequency is determined by the effective magnetic field B_{eff}, which is oriented at an angle θ_{eff} in the rotating frame. Since ω_{eff} is influenced by both the spin-lock pulse (ω_1) and frequency offsets ($\Delta\omega$), slower processes are enhanced ranging from zero to a few thousand Hz, in contrast to T_1, which enhances processes close to the Larmor frequency at MHz [14]. Magnetization decay after an RF pulse with $\alpha = 90°$ is described as Eq. 2.9, where t_{SL} is the duration of the spin-lock pulse:

$$\begin{aligned} M_x(t_{SL}) &= M_0 \cdot e^{-\frac{t_{SL}}{T_{1\rho}}} \\ &= M_0 \cdot e^{-t_{SL} \cdot R_{1\rho}} \end{aligned} \tag{2.9}$$

The magnetization evolution under a continuous spin-lock pulse can be modeled with the Bloch equations following [27], where the M_x can be used in the mono-exponential fit of Eq. 2.9 to extract $T_{1\rho}$:

$$\begin{aligned} \frac{dM_x(t)}{dt} &= \Delta\omega_0 M_y(t) - R_2 M_x(t) \\ \frac{dM_y(t)}{dt} &= -\Delta\omega_0 M_x(t) - R_2 M_y(t) + \omega_1 M_z(t) \\ \frac{dM_z(t)}{dt} &= -\omega_1 M_y(t) + R_1[M_0 - M_z(t)] \end{aligned} \tag{2.10}$$

Here, M (M_x, M_y M_z) is the magnetization vector, ω_1 is the frequency of the spin-lock pulse, $\Delta\omega_0$ is the frequency offset to the Larmor frequency, $R_1 = \frac{1}{T_1}$ is the longitudinal relaxation rate, $R_2 = \frac{1}{T_2}$ is the transverse relaxation rate and M_0 is the magnetization in thermal equilibrium. $\Delta\omega_0$ plays a crucial role in microstructure detection, as will be discussed in detail in the next section.

2.3. Microstructure detection

Microstructures can be detected on a sub-voxel level due to their influence on signal decay. Microstructure environments drive the decay of nuclear magnetic resonance signals with two key phenomena. First, microstructures perturb the magnetic field, which leads to locally varying offsets to the Larmor frequency, $\Delta\omega_0$. Second, spin-bearing particles diffuse through these susceptibility gradients, which leads to a loss of phase coherence. The geometry of the microstructure affects how this phenomenon contributes to the MR signal. Subsequent sections elaborate on these phenomena, focusing on spherical perturber geometries that resemble iron deposits [1, 2], lung alveoli [3], and exogenous contrast agents [5] .

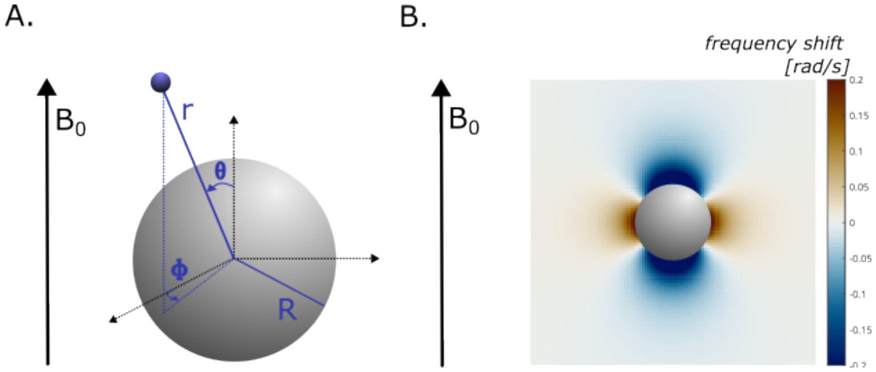

Figure 2.2: A) Spherical magnetic perturber (gray) with radius R. A single hydrogen spin (blue) diffuses around it. At time t, the location of the hydrogen spin may be described in spherical coordinates (r, θ, ϕ). B) When a perturber is placed in a magnetic field, an intrinsic susceptibility gradient is produced that affects the local Larmor frequency. The frequency shift is described as Eq. 2.11.

Microstructures perturb the magnetic field due to an intrinsic magnetic susceptibility difference to its surroundings. In the extended Bloch equations, this is represented as $\Delta\omega_0$ (Eq. 2.10). The geometry of the perturbing microstructures affects the magnitude and spatial extent of the produced field perturbations [13]. For the case of a homogeneously magnetized spherical perturber, the magnetic field is that of a magnetic dipole. The associated offset it causes to the Larmor frequency can be described in spherical coordinates with Eq. 2.11, where r is the distance of a spin to the center of a perturber, θ is the angle between the position vector and B_0, and R_i is the radius of a spherical structure [28], also illustrated in Fig. 2.2:

$$\omega(r) = \delta\omega R_i^3 \frac{3cos^2(\theta) - 1}{r^3} \tag{2.11}$$

In Eq. 2.11, $\delta\omega = \frac{1}{3}\gamma\Delta\chi B_0$ is the equatorial frequency shift of a sphere of radius R_i, where γ is the gyromagnetic ratio and $\Delta\chi$ is the susceptibility difference between the spherical object and the surrounding medium. The local Larmor frequency can be obtained by summing the contributions from multiple perturbers, where B_0 is the external magnetic field, ω_n is the field shift due to the *n*th perturber and $(r - r_n)$ is the distance from a spin to the *n*th perturber [29]:

$$\omega(r) = \gamma \cdot B_0 + \sum_n \omega_n(r - r_n) \tag{2.12}$$

The degree to which a spatially varying local Larmor frequency enhances spin dephasing depends on the amount of spin diffusion with respect to the size of the field fluctuations. The correlation time τ, which is in the order of R^2/D, describes the characteristic time scale associated with the fluctuations of the local magnetic field [30]. Minimal diffusion with respect to the correlation time leads to signal loss that can be reversed with a refocusing pulse, referred to as the static dephasing regime. In the static dephasing regime, magnetic heterogeneity in the sample shortens the T_2^* but does not affect the T_2 [12]. Motional narrowing occurs when the diffusion time is considerably longer than the correlation time, causing all spins to experience an average $\Delta\omega_0$ [29]. As a result, the relaxation times T_2^* and T_2 are not reduced [12, 30]. The regime between static dephasing and motional narrowing sensitizes the signal to the effects of diffusion with an irreversible loss of phase coherence characteristic to the perturber size [31]. Although the effect of diffusion is not included in the extended Bloch equations (Eq. 2.10), a generalization of the Bloch equation from Eq. 2.5 exists that has an added term for the effects of diffusion, named the Bloch-Torrey equation [32]:

$$\frac{\delta}{\delta t} m(r, t) = [D\Delta - i\omega(r)]m(r, t), \tag{2.13}$$

where $m(r, t) = m_x(r, t) + im_y(r, t)$ is the complex-valued local magnetization, $r = (r, \phi)$ is the position in polar coordinates, $\Delta = \delta_r^2 + r^{-1}\delta_r + r^{-2}\delta_r^2$ represents the two-dimensional Laplace operator, D is the diffusion coefficient and ω is the Larmor frequency. The Bloch-Torrey equation represents challenges for analytical solutions, and exact mathematical solutions are often limited to simplified models or extreme scenarios [30, 33].

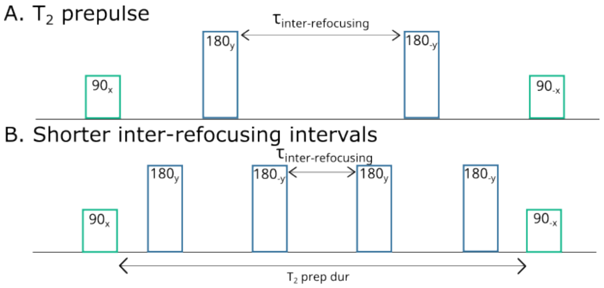

Figure 2.3: Sequence diagram of a standard T_2 sequence. The magnetization is refocused with a varying number of refocusing pulses, adjusting the ratio of diffusion time to correlation time, where the latter is characteristic to the perturber size.

Alternatively, the Bloch-Torrey equation can be solved numerically with a Monte Carlo approach, where diffusion is modeled as numerous spins subjected to random-walk, and the magnetization is averaged over many realizations.

By similarly extending the Bloch equations in Eq. 2.10 with a Monte Carlo approach, the combined effects of magnetic susceptibility and molecular diffusion can be investigated in microstructure environments. To quantify the spatial properties of microstructures, understanding the interplay between these two effects is essential. Both T_2 and $T_{1\rho}$ are sensitive to diffusion-mediated dephasing and can therefore be used to study microstructure environments. T_2 has been studied extensively and can investigate microstructure size through varying the time between refocusing pulses, probing the regime between static dephasing and the motional narrowing limit [29]. An MR pulse sequence utilizing T_2 decay with various inter-refocusing times is illustrated in Fig. 2.3. The following section will elaborate on how $T_{1\rho}$ relaxation can probe microstructures.

2.3.1. $\mathbf{T_{1\rho}}$ as microstructure probe

$T_{1\rho}$ relaxation is a less studied method for investigating diffusion through susceptibility gradients, though it shows promising results *in vivo* [20]. The spatial frequency of the field variations can be investigated with spin-lock frequency, similar to probing correlation time with inter-refocusing pulse interval. Intrinsic properties that affect $T_{1\rho}$ relaxation are macromolecule interactions, such as chemical exchange, and motional processes, such as diffusion (Fig. 2.4 and Eq. 2.14) [15, 20]. At f_{SL} = 0 Hz, $R_{1\rho}$ approaches the transverse relaxation rate R_2. Low f_{SL} emphasize the effects of diffusion ($R_{1\rho}^{\text{Diff}}$), which can be sensitized to susceptibility gradients surrounding microstructures. A higher f_{SL} is sensitive to chemical exchange processes ($R_{1\rho}^{\text{Ex}}$), which is mainly affected by the exchange rate of hydroxyl, amine, and amide protons as well as the chemical shift of the exchanging species [15]. Beyond a maximum f_{SL} the signal is no longer expected to be sensitive to chemical exchange processes and reflects the intrinsic transverse relaxation rate between tissue and water (R_{2w}) [20].

$$R_{1\rho} = R_{1\rho}^{\text{Diff}} + R_{1\rho}^{\text{Ex}} + R_{2w} \tag{2.14}$$

Imaging over a range of spin-lock frequencies provides an $R_{1\rho}$ dispersion profile (Fig. 2.4). The midpoint of regions where the dispersion is strongest is expected to correspond to the appropriate diffusive or chemical exchange rate. The second derivative of the $R_{1\rho}$ curve provides three inflection points, which correspond to the mean diffusive rate, the mean chemical exchange rate, and the midpoint between the two processes [15]. Since diffusion around magnetic perturbers provides information on the microstructures causing the magnetic inhomogeneities, the work in this thesis focused on $R_{1\rho}^{\text{Diff}}$.

Few studies have explored an explicit expression for $R_{1\rho}^{\text{Diff}}$. When assuming the susceptibility gradient caused by a perturber to be of a singular sinusoidal spatial frequency, $R_{1\rho}^{\text{Diff}}$ can be described as [15]:

$$R_{1\rho}^{\text{Diff}} = \frac{\gamma^2 g^2 D}{(q^2 D)^2 + \omega_1^2} \tag{2.15}$$

Here, q is the spatial frequency, γ is the gyromagnetic ratio, g is the mean gradient strength, D is the diffusion coefficient, and ω_1 is the spin-lock frequency.

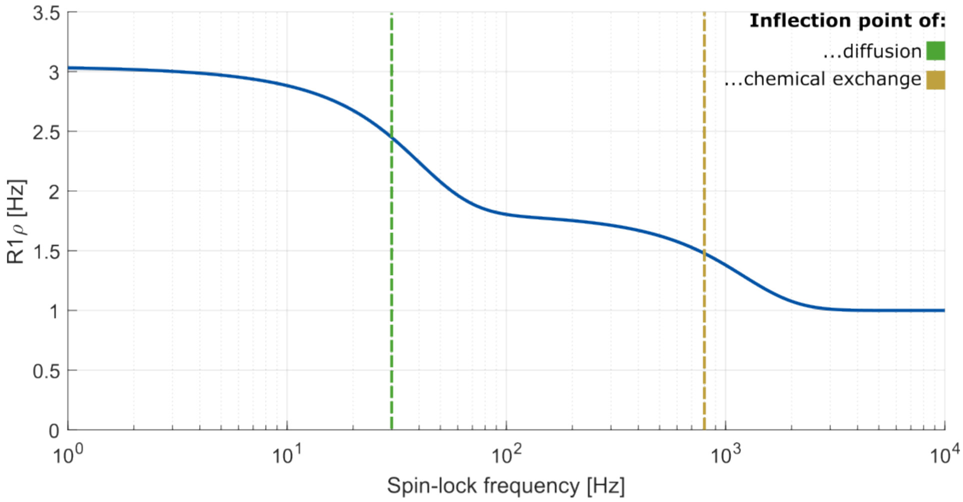

Figure 2.4: $R_{1\rho}$ dispersion plot based on [15]. The dispersion profile is a combination of the diffusion component, the chemical exchange component and the transverse relaxation rate between tissue and water. The first dashed line (green) highlights the rate where the signal is most sensitive to diffusional processes, whilst the second (yellow) dashed line highlights the rate most sensitive to chemical exchange. The final plateau represents the intrinsic transverse relaxation rate between tissue and water, where the signal is no longer sensitive to either diffusion or chemical exchange.

$$R_{1\rho}^{\text{Diff}} = \gamma^2 g^2 D \cdot \frac{\tau_c^2}{1+\omega^2\tau_c^2} \tag{2.16}$$

In Eq. 2.16, the correlation time is defined as $\tau_c = 1/(q^2 D)$, and it is inversely related to the characteristic locking field frequency, $w_c = 1/\tau_c$. The correlation time is dependent on the spatial scale of the inhomogeneities and is not influenced by the magnitude of the susceptibility variations [34]. At the inflection point of the dispersion, the period of spin nutation matches the time required for a spin to diffuse through the characteristic dimension of the perturber. According to Eq. 2.15 this is expected to occur at $\omega_1^{\text{inflection}} = 1/(\sqrt{3}\tau_c)$ [34].

2.3.2. Measuring $\mathbf{T_{1\rho}}$

The $T_{1\rho}$ value of a tissue can be measured with a pulse sequence locking the magnetization in the transverse plane (Fig. 2.5). In an SL module, the longitudinal magnetization is tipped into the transverse plane with an initial RF pulse. A subsequent continuous RF pulse effectively locks the magnetization in the transverse plane, during which time $T_{1\rho}$ relaxation occurs [35]. The SL pulse is aligned with the net magnetization vector, has an amplitude B_1, is applied for a duration called the spin-lock time (t_{SL}), and is not slice selective [36, 37]. It is included into the Bloch equations (Eq. 2.10) as ω_1. Afterward, the magnetization is flipped back to the longitudinal plane by a third RF pulse and the residual transverse relaxation is crushed with a gradient crusher [38]. The now relaxed longitudinal magnetization is imaged with an imaging module.

The classical SL module as illustrated in Fig. 2.5 is greatly influenced by B_0 and B_1 field inhomogeneities. B_1 inhomogeneities lead to imperfect excitation and spin-locking, while B_0 inhomogeneities lead to an off-resonant application of the SL pulse causing the locked magnetization vector to precess around an effective B_{eff}. The produced banding artifacts in the image are t_{SL} and f_{SL} dependent, thus inhibiting the accurate measurement of $T_{1\rho}$ in quantitative imaging [12, 39]. Several adaptations to the SL prepulse have been proposed to increase the resilience to field imperfections [39]. Approaches as the rotary echo [36], composite SL [40] and balanced SL module [39] aim to reduce B_1 artifacts through phase balancing and B_0 artifacts with refocusing pulses.

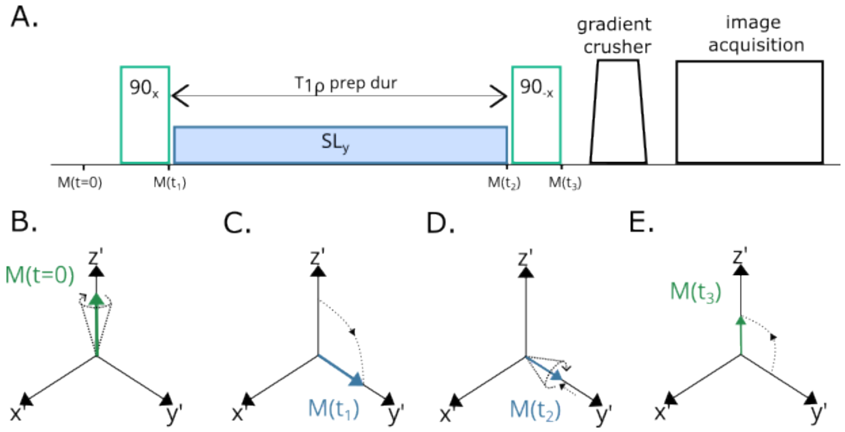

Figure 2.5: A) Sequence diagram of a standard spin-lock pulse sequence. After tipping M away from the longitudinal plane, it is locked in the transverse plane with a continuous RF pulse, during which time $T_{1\rho}$ relaxation occurs. M is nutated back and residual transverse magnetization is crushed with a gradient crusher. The now relaxed M_z is imaged with an image acquisition sequence. B-E) The dynamics of the net magnetization vector M when exposed to a standard spin-lock pulse sequence at times corresponding to illustrated prepulse.

3
Methods

Simulation and phantom experiments were performed to investigate the reliability of detecting microstructures with a spin-lock pulse sequence. This chapter elaborates on the implementation of the simulation and on the experimental design of the phantom experiments.

3.1. Simulations

The temporal evolution of the magnetization vector M under a spin-lock pulse sequence was modeled with Eq. 2.10, where the Bloch equation has been numerically solved with a Monte Carlo approach and the diffusion was added as a random walk [41]. The diffusion of individual spin-bearing particles is modeled with the following sequential steps:

1. A number of spins was randomly distributed throughout the simulation volume.
2. At each time step Δt, the spins moved randomly. The diffusion was stochastic and assumed to be isotropic, with a random displacement with mean 0 and a standard deviation of $\sqrt{2D\Delta t}$. D is the diffusion coefficient [8, 42]. The size of the time step ensured that the displacement within one time step was much smaller than the size of the magnetic perturbers.
3. The respective distance of each spin to the magnetic perturber was computed. The locally experienced magnetic field was calculated with Eq. 2.11.
4. The signal was calculated from the evolution of the magnetic moment using Eq. 2.10.

3.1.1. Implementation of simulation

A 3D extended Krogh capillary model was used to model a complex arrangement of spherical magnetic perturbers [30]. The model comprises a single spherical perturber placed at the center of a spherical volume, representing a repeating unit cell. The volume of the unit cell was determined by the volume fraction, η. The perturber was modeled as uniformly magnetized and impermeable [8, 30, 32, 34].

Boundary conditions were implemented to account for spins reaching the voxel edge and the perturber surface (Fig. 3.1). When a spin reaches the edge of the voxel, it was placed at the opposite side of the model imitating a spin entering the repeating unit cell from a neighboring voxel. At the surface of the spherical perturber, a spin was reflected by computing a new θ and ϕ and positioning it at the previous distance r from the center of the perturber.

The magnetization in the voxel was subjected to a conventional spin-lock sequence in MATLAB R2018b. It assumed a perfect $\pi/2$ initial hard pulse to tip the magnetization into the transverse plane (M_0 = 1) after which it was locked in the transverse plane with a continuous SL pulse. The model was simulated with locking frequencies of f_{SL} 0, 1, 3, 10, 30, 80, 140, 250, 500, 1000, and 3000 Hz and averaged over a total of 20,000 spin trajectories. The resulting signal was fit to the mathematical model of mono-exponential decay in Eq. 2.9 with a two-parameter fit on 15 equally spaced t_{SL} between 1 and 120 ms.

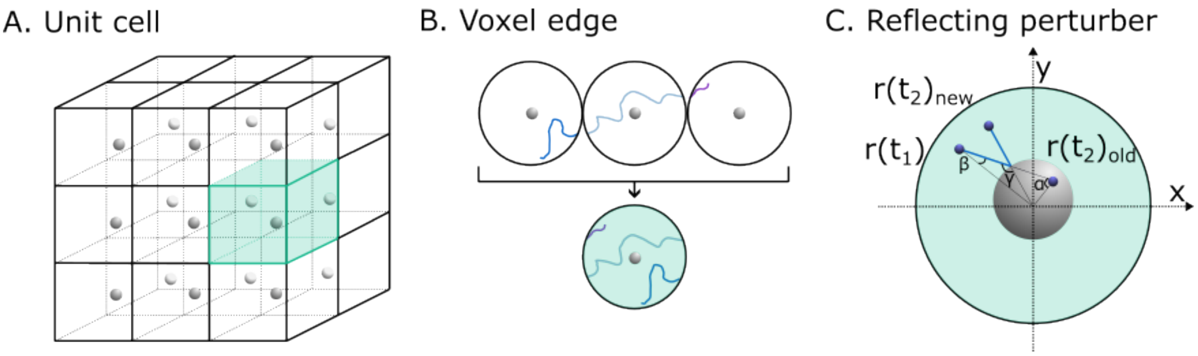

Figure 3.1: A) The simulated volume (green) was assumed to be a repeating unit cell with one spherical perturber (gray) at its center. The cubic unit cell was modeled as spherical to increase computational speed. B) When a spin enters a neighboring cell, it was modeled as entering its current cell with the path it would have taken in the neighboring cell. C) When a spin at distance r at time t_1 moved into the perturber at $t_{2,old}$, it was reflected to $r(t_2)_{new}$. A new θ and ϕ were computed and the spin was placed at the old distance r from the center of the spherical perturber.

3.2. Phantom experiments

Experiments were performed on a 3T Ingenia system (Philips, the Netherlands) to investigate the detection of microstructures *in phantom*. The following sections elaborate on the setup of the phantom experiments and the image acquisition that was performed.

3.2.1. Phantom construction

Microbeads

Polystyrene microbeads lacking a chemical exchange species were selected for isolating the effect of diffusion (NH_2-coated Micromer-M, Micromod, Germany). They were studied at bead diameters of 3, 10, and 20 μm for ensuring sensitivity in clinically feasible spin-lock frequencies [34].

Medium

Microbeads diluted in water tend to settle over time [34]. To ensure a uniform and reproducible dispersion, microbeads are often suspended in a gel matrix. In this thesis, the suitability of gelatin, agarose, and polyacrylamide was assessed for microstructure detection.

In addition to the gel matrix, the magnetic susceptibility difference was adjusted to enhance the field perturbation around a microstructure. A range of four susceptibility agents was tested for suitability in regard to magnetic properties and phantom fabrication, being gadolinium Dotarem (Gd), copper sulfate ($CuSo_4$), nickel chloride ($NiCl_2$) and holmium (III) chloride hexahydrate ($HoCl_3 \cdot 6H_20$).

Configuration

The vials were prepared according to the protocol in Appendix A as 1.8 mL dilutions containing microbeads, a gelling agent, and a susceptibility agent in a 2 mL plastic vial. The vial was submerged in a water bath secured in a 3D-printed holder to ensure a negligible susceptibility difference between the vial and the surroundings, thereby reducing susceptibility artifacts (Fig. 4.2) [43].

3.2.2. System verification

The system verification aimed to identify the experimental parameters of the phantom experiments and to evaluate the prepulse resilience to banding artifacts by investigating the effect of:

- the gelling agent on the diffusion coefficient, D,
- the susceptibility agents on the relaxation times T_1 and T_2,
- the susceptibility agents on the frequency shift, $\Delta\chi$,
- (non)-adiabatic refocusing pulses on banding artifacts.

Diffusion coefficient

The D was estimated to determine the influence of the gelling agent on spin diffusivity with a DWI sequence (Tab. 3.1). The signal from the images was fit to the equation below to extract the apparent diffusion coefficient (ADC) of water and of a medium of PA:

$$D = -\frac{1}{b} \cdot ln\frac{S_{DWI}}{S_{b=0}} \tag{3.1}$$

Table 3.1: Scan parameters utilized in acquiring DWI images for quantifying the effect of the gelling agent, read out with a spin echo - echo planar imaging (SE-EPI) sequence.

Scan type	**Image readout**	**FOV** [mm]	**Resolution** [mm]	**TR/TE** [ms]	**FA** [°]	**b-value** $[s/mm^2]$
DWI	SE-EPI	200x200x14	1.5x1.89x4	1000/68	90°	0, 300, 600

Volume magnetic susceptibility

The effect of the susceptibility agent on the magnetic susceptibility of the vials was assessed with a B_0 map (Tab. 3.2) following the validation of the measurement method in Appendix B. The map displayed the frequency shift to the Larmor frequency. The effect of the susceptibility agent was extracted by:

$$\Delta\Omega = B_{0,agent} - B_{0,ref}, \tag{3.2}$$

where $B_{0,ref}$ is the frequency map in the absence of a susceptibility agent and $B_{0,agent}$ in the presence of it. The frequency shift was related to the magnetic susceptibility of the vial with Eq. 3.3 [41]. Here, $\Omega_0 = 42.58MHz/T$ is the Larmor frequency of the hydrogen spin, θ is the angle of the vial to the static magnetic field, $\Delta\Omega$ is the shift caused by the susceptibility agent, and $\Delta\chi$ is the magnetic susceptibility of the vial as a whole. Because the vial was aligned with the static magnetic field, θ can be regarded as 0:

$$\begin{aligned}\Delta\Omega &= \frac{\Delta\chi_{vial}}{6}(3cos^2\theta - 1)\Omega_0 \\ &= \frac{\Delta\chi_{vial}}{3}\Omega_0, \quad for \quad \theta = 0,\end{aligned} \tag{3.3}$$

Table 3.2: Scan parameters utilized in B_0 maps for quantifying the effect of the susceptibility agents, acquired with a fast field (gradient) echo (FFE).

Scan type	**Image readout**	**FOV** [mm]	**Resolution** [mm]	**TR/TE** [ms]	**FA** [°]	**dTE** [ms]
B_0 map	3D FFE	130x130x8	1x1x1	30/5.5	10	1

T1 and T2 maps

The effect of the susceptibility agent on the medium was determined by mapping the magnetic properties T_1 and T_2 with scan parameters summarized in Tab. 3.3.

Table 3.3: Scan parameters utilized in T_1 and T_2 maps for quantifying the effect of the susceptibility agents. The T_1 map is acquired with a fast field (gradient) echo (FFE) and the T_2 map with a gradient and spin echo (GraSE).

Scan type	**Image readout**	**FOV** [mm]	**Resolution** [mm]	**TR/TE** [ms]	**FA** [°]
T_1 map	2D Balanced FFE	130x130x10	2x2x10	2.2/0.99	20
T_2 map	2D GraSE	130x130x10	2x2x10	1000/n*10.24, n=9 echos	90

Spin-lock prepulse evaluation

The prepulses implemented in this study aimed to reduce banding artifacts with extensive phase balancing combined with either adiabatic or non-adiabatic refocusing pulses following [44], illustrated in Fig. 3.2. Different from a regular on-resonance block pulse, an adiabatic pulse sweeps the magnetization over a range of frequencies with a modulated pulse amplitude. Adiabatic pulses are resilient to B_1 inhomogeneities of the refocusing pulse, providing more optimal refocusing for B_0 inhomogeneities. Following an evaluation of the prepulses at a range of f_{SL}, the prepulse with adiabatic refocusing was selected for microstructure detection.

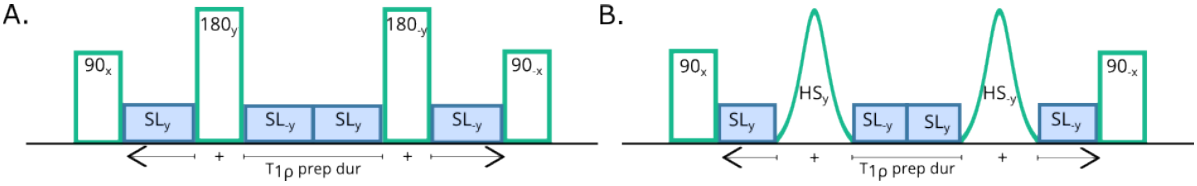

Figure 3.2: Adaptations to the standard SL prepulse implemented in this thesis with non-adiabatic refocusing (A) and adiabatic refocusing (B). Both prepulses provide resilience against B_1 imperfections by phase balancing and against B_0 imperfections by refocusing pulses. Adiabatic refocusing pulses are designed to provide a more optimal B_0 resilience.

3.2.3. Spin-lock imaging

The prepulse as illustrated in Fig. 3.2B was elected to quantify the $T_{1\rho}$ in phantom experiments with microbeads. To generate dispersion graphs, scans were acquired at a range of f_{SL} of 80, 100, 150, 200 and 400 Hz with scan parameters as summarized in Tab. 3.4. Each scan comprised two time dynamics used to extract the $R_{1\rho}$, being a reference image without a spin-lock prepulse (t_{SL} = 0 ms), and an image with a spin-lock prepulse (t_{SL} = 30 ms).

Table 3.4: Scan parameters utilized in microstructure detection with $T_{1\rho}$. The images were acquired with a turbo field (gradient) echo (TFE).

Scan type	**Image read-out**	**FOV** [mm]	**Resolution** [mm]	**TR/TE** [ms]	**FA** [°]	**M_z recovery** [ms]
$T_{1\rho}$	T_1-weighted 2D TFE	130x130x8	1x0.98x8	3.1 / 1.55	10	3000

4

Results

The results from simulation and phantom experiments illustrated the possibility of detecting microstructures with a spin-lock pulse sequence. The simulations primarily exhibited the influence of several microstructure characteristics on the relaxation rate, while phantom data presented to what extent microstructures can be detected with the current experimental design.

4.1. Simulation

The simulation results demonstrated how several characteristics of microstructures alter the $R_{1\rho}$ dispersion profile. In separate simulation experiments, the effects of microstructure radius, concentration, susceptibility difference, and spin diffusivity were assessed with the parameter set summarized in Tab. 4.1. Throughout these experiments all other parameters were maintained at a constant value indicated in bold.

Table 4.1: Parameters used in simulation experiments, where 1χ = -1.21 $\cdot 10^{-7}$ and bold printed numbers represent the parameter at its constant value. Parameters were chosen to resemble [34]. The range of D was extended from a clinically relevant value of 2.3 $10^{-6} mm^2/ms$ to investigate various diffusion regimes.

Parameter	**Unit**	**Values**
R	μm	0.5, 1, 2.5, 4, **5**, 6, 7.5, 10, 20, 50
η	-	0.005, 0.010, 0.015, **0.020**
$\delta\chi$	-	**1**χ, 2χ, 3χ, 4χ
D	$10^{-6} mm^2/ms$	10^{-6}, 10^{-3}, **2.3**, 10^{3}
T_1	ms	2597
T_2	ms	1200
Δt	μs	0.4
B_0	T	3

The $R_{1\rho}$ dispersion plots generated from simulation experiments are illustrated in Fig. 4.1. Each plot displays the influence of an individual parameter on the relaxation rate. In general, microstructures induced a characteristic profile with an initial plateau at low and high spin-lock frequencies connected through a slope steepest at the inflection point. In Fig.4.1A, the influence of the microstructure radius was illustrated. The radius contributed to the relaxation rate by altering both the dispersion magnitude and the inflection point. An increase in radius produced a higher plateau at low spin-lock frequencies for a specific range of radii, thereby indicating an increased relaxation rate. Additionally, larger microstructures shifted the position of the inflection point to lower frequencies. Fig.4.1B displays the effect of the microbead concentration. Within the range of simulated concentrations, more closely spaced microstructures accelerated the relaxation at low spin-lock frequencies, though the inflection point remained at the original position. The susceptibility difference influenced the relaxation rate in a similar manner, as visible from Fig.4.1C. The amount of spin diffusivity altered the profile through a more complex mechanism, where both the dispersion magnitude and the inflection point were affected (Fig.4.1D). The behavior indicated that the order of diffusion influences the size-selectivity of $T_{1\rho}$

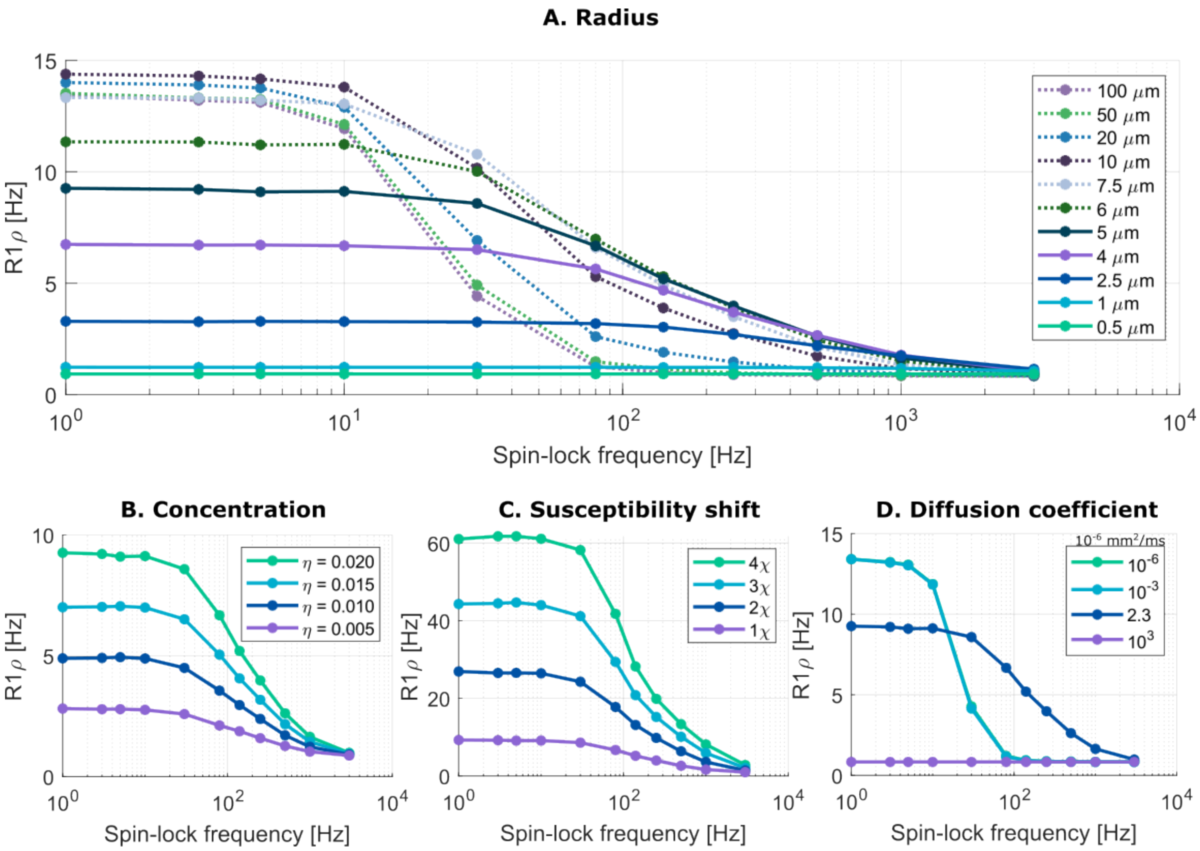

Figure 4.1: Simulation results. The used parameter set was summarized in Tab. 4.1, where bold print indicates fixed parameter values. A) The effect of perturber radius on the $R_{1\rho}$ dispersion profile. Solid lines represent beads smaller than 5 μm, whereas dotted lines are larger beads. B) The effect of perturber concentration. Since the simulation consisted of one perturber in a spherical volume, a change in concentration was achieved with a change in simulation volume. C) The effect of the susceptibility shift, where $1\chi = -1.21 \cdot 10^{-7}$. D) The effect of varying the diffusion coefficient.

4.2. Phantom experiments

Microbeads were suspended in a polyacrylamide gel to demonstrate the effect on the relaxation rate *in phantom*. Independent measurements were performed to verify the suitability of gelling and susceptibility agents by measuring experimental parameters of diffusion, T_1, T_2, and frequency shift $\Delta\Omega$. Afterward, microstructure detection was evaluated with a spin-lock pulse sequence.

4.2.1. System verification

Gelling agents

The suitability of gelatin, agarose, and polyacrylamide in microstructure detection was investigated to determine the optimal phantom configuration. Despite gelatin and agarose being common gelling agents in MR, specific properties rendered them unsuitable for microstructure characterization. Gelatin gels tended to contain air bubbles which interfered with microstructure detection due to their comparable size and magnetic susceptibility [43]. Agarose was less susceptible to trapping air, yet it dramatically reduced the T_2 diminishing the relative contribution of the microstructures [45]. Given the limitations of both gelatin and agarose, polyacrylamide was used as alternative gelling agent [10]. It demonstrated both a longer T_2 - approximately 1900 ms at 10% concentration compared to 150 ms for 1% agarose [45] - and exhibited a lower tendency to trap air bubbles. Despite its advantages, polyacrylamide did lead to a slightly decreased diffusion coefficient as compared with agarose gels [45]. Based on these considerations, a gel with a concentration of 9% polyacrylamide was selected.

The diffusion of spins was dependent on properties of the gelling agent. The effect of polyacrylamide gel on the spin diffusivity was assessed with an ADC map. The ADC values of a vial with 9% PA were shown in Figure 4.2B. The mean ADC value in a rectangular ROI in the center of the vial was 1.94 $\cdot 10^{-6}$ mm^2/ms. The mean ADC value of an ROI in the water surrounding the vial was 2.06 $\cdot 10^{-6}$ mm^2/ms.

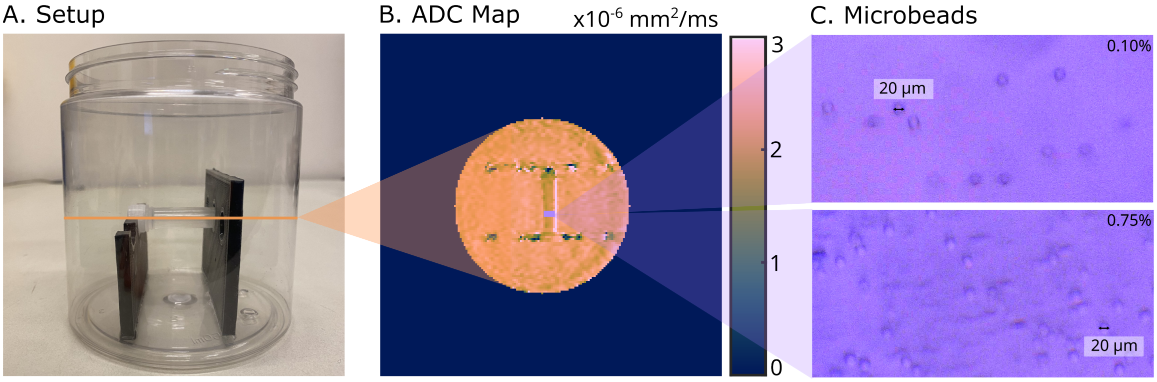

Figure 4.2: A) Setup of phantom experiments with microbeads with a radius of 10 μm suspended in a 9% PA solution submerged in a water bath. B) ADC map of a vial without microbeads in coronal orientation. The ADC was only minimally affected by the PA gel. C) Microscope images of the microbeads at varying concentrations.

Susceptibility agents

The addition of a susceptibility agent aided microstructure detection by enhancing the intrinsic susceptibility gradient around a perturber. As the difference in magnetic susceptibility between the microstructures and the surrounding medium increases the experienced frequency shift, spin dephasing was enhanced. Therefore, it was crucial to understand the relation between the susceptibility agent concentration and the frequency shift along with their suitability in phantom fabrication. Following the verification of the measurement method (Appendix B), the magnetic properties and the production suitability of $HoCl_3 \cdot 6H_20$, $CuSo_4$, $NiCl_2$ and Gd were investigated. The $\Delta\Omega$, T_1, T_2, and the effect on the gelling of polyacrylamide were summarized in Tab. 4.2.

It was essential that the agents enhance the effect of the susceptibility gradient while minimizing significant reductions in T_1 and T_2 relaxation times. Additionally, they should not interfere with the gelling process of PA. The agent with the largest effect on the susceptibility shift with a limited reduction in dipole relaxivity was $HoCl_3 \cdot 6H_20$. However, polystyrene microbead aggregations formed when the gel matrix included holmium (Appendix C). $CuSo_4$ prolonged the gelling process of PA from a minute to more than a day. Finally, both $NiCl_2$ and Gd had a considerable effect on the susceptibility shift yet additionally reduced the dipole relaxivity. Since $NiCl_2$ experienced a color-changing chemical reaction and gadolinium provided possibilities in subsequent *in vivo* experiments, gadolinium was selected as a susceptibility agent for the phantom experiments.

Table 4.2: Comparison of the susceptibility agents $HoCl_3 \cdot 6H_20$, $CuSo_4$, $NiCl_2$ and $Gd\ Dotarem$. The effects on the magnetic properties and the gelling process of polyacrylamide were included in the comparison.

Susceptibility agent	**Concentration**	**Frequency shift [Hz]**	**T_1 [ms]**	**T_2 [ms]**	**Effect on gelling**
$HoCl_3 \cdot 6H_20$	5 mM	114	493	528	Bead aggregations
	10 mM	206	281	350	
$CuSo_4$	4 mM	-	-	-	Slows gelling to > 24h
	8 mM	-	-	-	
$NiCl_2$	3 mM	8	1100	750	Chemical reaction
	6 mM	22	750	450	
$Gd\ Dotarem$	0.15 v/v%	14	680	192	None
	0.30 v/v%	31	212	110	

Spin-lock prepulse evaluation

Spin-lock preparatory modules with non-adiabatic and adiabatic refocusing were evaluated for their resilience against B_0 and B_1 imperfections. Images were acquired at various t_{SL} and f_{SL} with scan parameters as described in Tab. 3.4. At 0 Hz, the prepulse with non-adiabatic refocusing displayed significant banding artifacts increasing with spin-lock duration that are less pronounced in the adiabatic refocusing prepulse. The banding artifacts diminished with higher f_{SL}. The prepulse with adiabatic refocusing pulses was utilized in phantom experiments with microbeads.

A. Varying t_{sl} for f_{sl} = 0 Hz

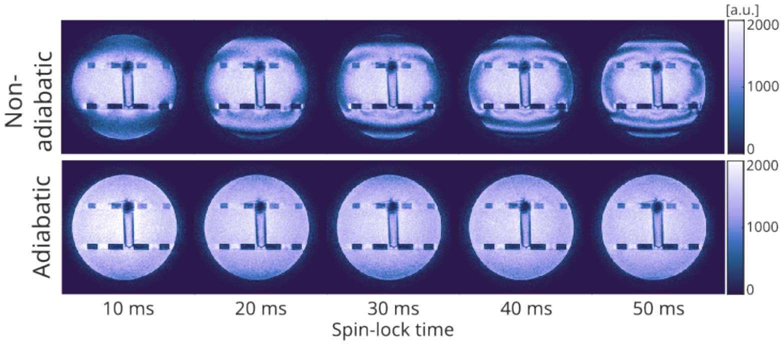

B. Varying f_{sl} for t_{sl} = 50 ms

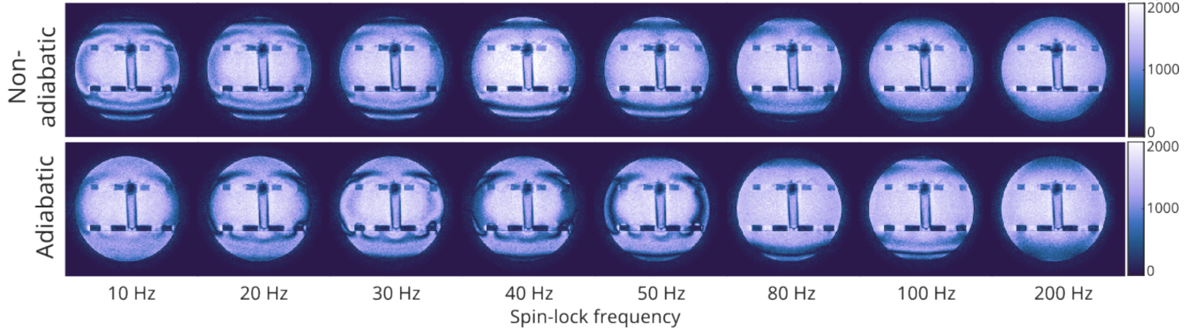

Figure 4.3: Evaluation of the implemented spin-lock pulse sequences from Fig. 3.2 to facilitate a comparison between adiabatic and non-adiabatic refocusing pulses. A) Signal magnitude images acquired with f_{sl} = 0 Hz and a range of t_{sl}. B) Signal magnitude images acquired at t_{sl} = 50 ms and a range of f_{sl}.

4.2.2. Microstructure detection

After system verification, phantom experiments were conducted to evaluate the detection of microstructures with a spin-lock pulse sequence. Vials were fabricated as summarized in Tab. 4.3 to address the following objectives:

- to investigate the effect of microbead concentration of 3 μm beads (set 1),
- to investigate the effect of microbead concentration of 10 μm beads (set 2),
- to investigate the effect of microbead concentration of 10 μm beads in the absence of Gd (set 3),
- to monitor whether signal evolution under the SL pulse is mono-exponential (set 4),
- to evaluate the reproducibility of phantom fabrication with Gd (set 5),

Table 4.3: Vials used in phantom experiments. The first three sets aimed to investigate the effect of microbead concentration on the signal acquired with an SL pulse sequence. Set 4 was imaged to monitor the mono-exponential behavior of signal decay. Set 5 assessed the reproducibility of the phantom fabrication process. Scans were acquired with 5 repetitions (set 1-4) or with 10 repetitions (set 5).

	Polyacrylamide [%]	**Gadolinium [%]**	**Microbead radius [μm]**	**Microbead concentration [%]**
set 1	9	0.3	3	0.0, 0.5, 1.0, 1.5, 2.0
set 2	9	0.3	10	0.0, 0.5, 1.0, 1.5, 2.0
set 3	9	0.0	10	0.0, 0.5, 1.0, 1.5, 2.0
set 4	9	0.3	10	0.0, 2.0
set 5	9	0.3	20	0.0 × 5, 1.0 × 5

The phantom results were compared to simulation experiments with parameters based on the outcomes of the system identification (Tab. 4.4).

Table 4.4: Parameters used in simulation experiments for comparison to phantom experiments. The susceptibility difference, T_1 and T_2 values were adjusted to suit the conditions with and without gadolinium.

Parameter	Unit	Values
R	μm	3, 10
η	-	0.005, 0.010, 0.015, 0.020
$\delta\chi$, $\delta\chi_{gd}$	-	$-1\cdot10^{-7}$, $-5\cdot10^{-7}$
T_1, $T_{1,gd}$	ms	2300, 210
T_2, $T_{2,gd}$	ms	1900, 62
D	$10^{-6}\ mm^2/ms$	2.0
Δt	μs	0.4
B_0	T	3

Fig. 4.4A illustrates the results obtained to address the first aim of the phantom experiments: how varying the concentration of 3 μm beads affected the $R_{1\rho}$ dispersion profile with an enhanced susceptibility difference caused by 0.3% Gd. The resultant signal and $R_{1\rho}$ dispersion plot for an f_{SL} of 80, 100, 150, 200, and 400 Hz at a t_{SL} of 30 ms with a mean and standard deviation of 5 scan repetitions per vial was displayed. For reference, the images at t_{SL} = 30 ms normalized to t_{SL} = 0 ms corresponding to the 2.0% microbeads vial were displayed above the phantom signal plot. The relaxation rate for different microbead concentrations differed minimally and the order was inconsistent. The resultant dispersion plot was compared to simulation results, where the dispersion magnitude was small though an increase in microbead concentration led to a consistent increase in relaxation rate.

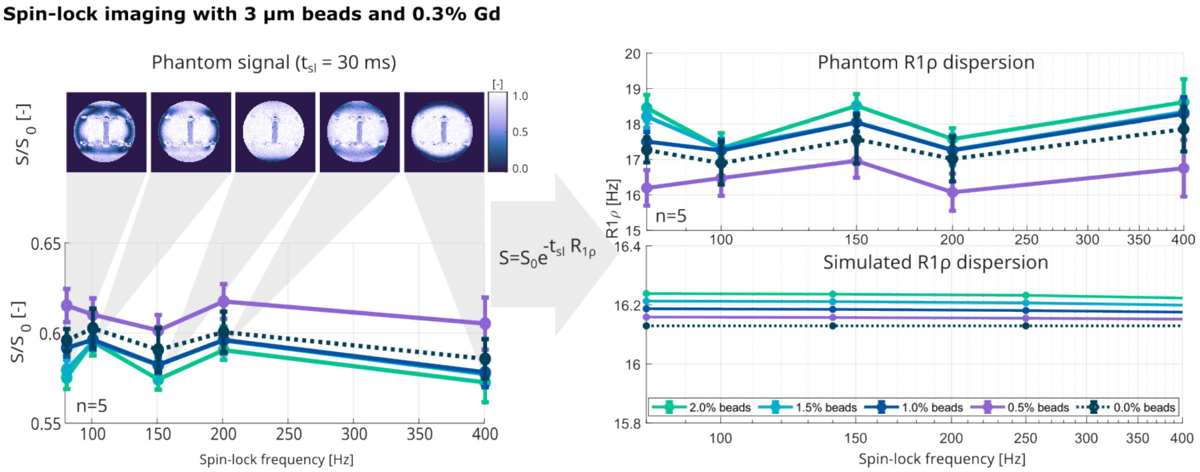

Figure 4.4: Phantom experiments to determine the effect of 3 μm bead concentration on the signal (left) and on $R_{1\rho}$ (right) in a medium of 9% PA and 0.3% Gd. Signal images at t_{SL} = 30 ms normalized to t_{SL} = 0 ms of the 2.0% beads are shown for reference. The data points represent an average of five repetitions and the error bars represent ± one standard deviation. Both experimental and simulated data are shown.

To investigate the effect of microbead radius in phantom, experiments were repeated with 10 μm beads and 0.3% Gd. The signal, $R_{1\rho}$ dispersion and simulation plots for a range of 10 μm microbead concentrations with gadolinium were shown in Fig. 4.5. The simulation predicted a slight dispersion magnitude with step-wise increase in relaxation rate of an increase in bead concentration. However, the gradual and consistent increase in relaxation rate could not be captured in phantom data.

Spin-lock imaging with 10 μm beads and 0.3% Gd

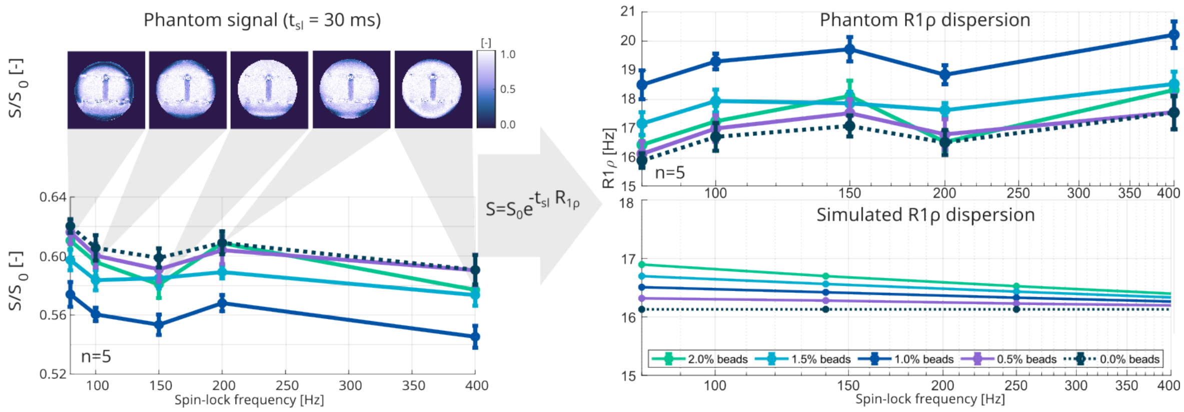

Figure 4.5: Phantom experiments to determine the effect of 10 μm bead concentration on the signal (left) and on $R_{1\rho}$ (right)in a medium of 9% PA and 0.3% Gd. Signal images at t_{SL} = 30 ms normalized to t_{SL} = 0 ms of the 2.0% beads are shown for reference. The data points represent an average of five repetitions and the error bars represent ± one standard deviation. Both experimental and simulated data are shown.

When comparing the results of 3 μm beads and 10 μm beads, as was shown in Fig. 4.6 for 0%, 1% and 2% microbeads, simulated data predicted minimal effect of the microbeads on the relaxation rate and experimental data did not display a characteristic dispersion profile.

The effect of microbead radius

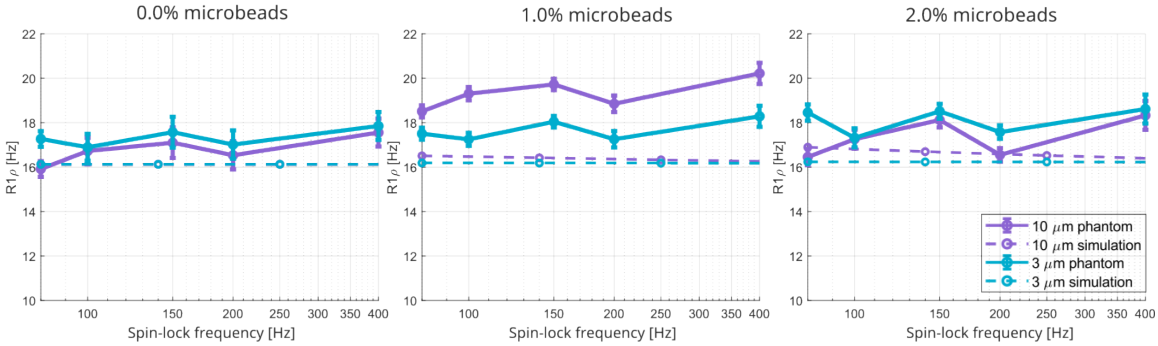

Figure 4.6: Comparison of radius and concentration effects in phantom data (solid lines) and simulated data (dashed lines). Results are shown for 3 and 10 μm microbeads in 9% PA with 0.3% Gd.

The influence of a lower susceptibility shift was investigated by imaging a set of vials with 10 μm microbeads lacking Gd as susceptibility agent. Fig. 4.7 visualizes signal dephasing due to a weaker susceptibility gradient. The system experienced negligible signal decay in the duration of the spin-lock preparation rendering the fit of the relaxation rate unstable.

In an additional experiment, the behavior of signal decay was monitored. As the calculation of the relaxation rate depended on fitting the signal to a mathematical model of mono-exponential decay, it was crucial to ensure that the phantom data adhered to it. A scan mapping the signal over the course of 30 ms with a dt of 5 ms normalized to the first-time dynamic provided insights into the signal decay behavior at an f_{SL} of 0, 200, and 400 Hz. From Fig. 4.8, it could be deduced that for 10 μm microbeads in 0.3% Gd the signal behaved as expected.

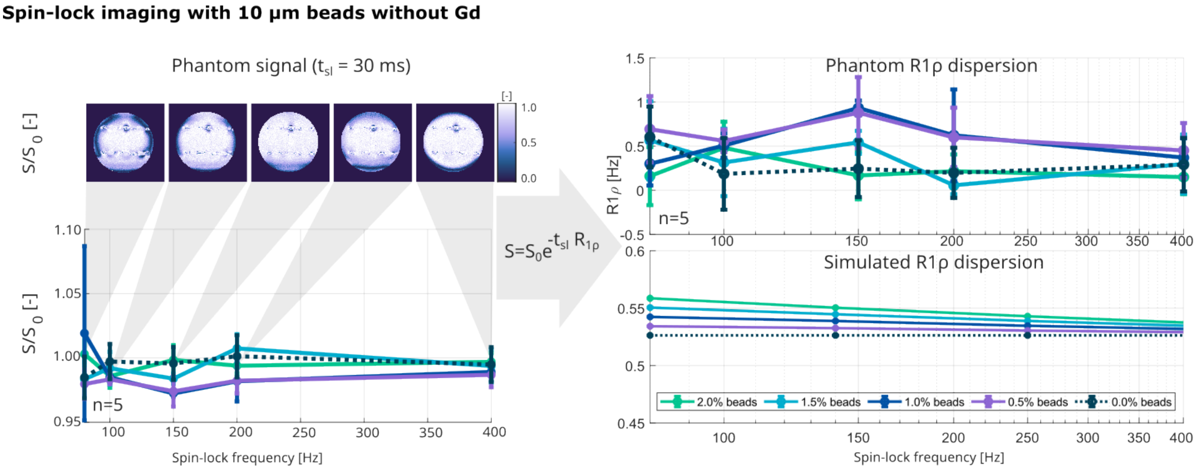

Figure 4.7: Phantom experiments to determine effect of 10 μm bead concentration on the signal (left) and on $R_{1\rho}$ (right) in a medium of 9% PA. Signal images at t_{SL} = 30 ms normalized to t_{SL} = 0 ms of the 2.0% beads are shown for reference. The data points represent an average of five repetitions, and the error bars represent ± one standard deviation. Both experimental and simulated data are shown.

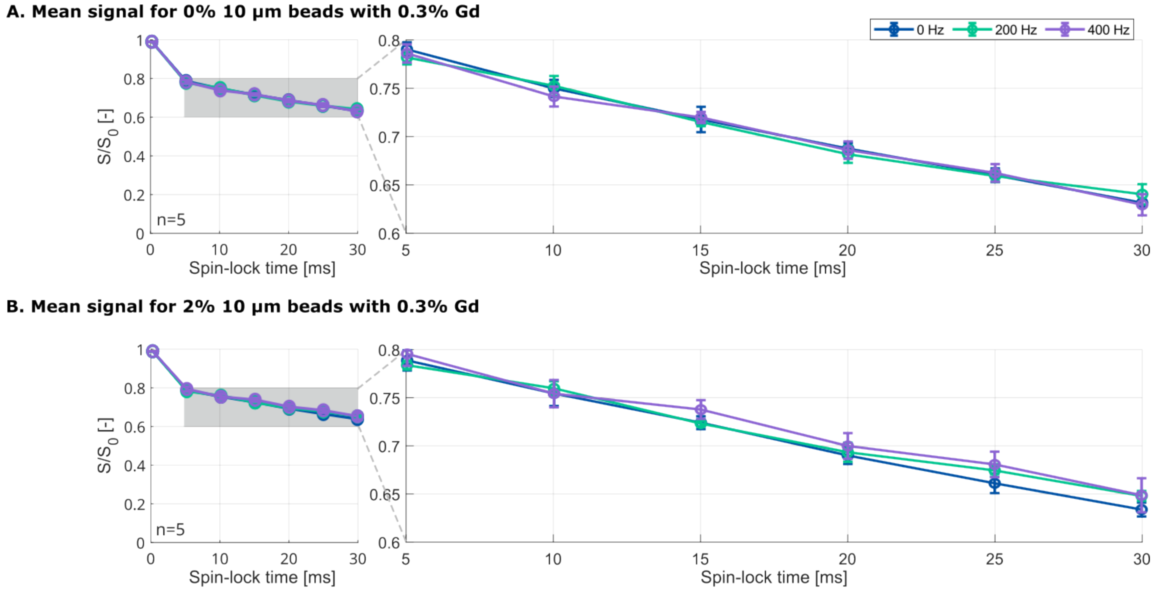

Figure 4.8: Signal decay of a reference vial (A) and a vial with 2% 10 μm beads (B). The signal was measured at 5 ms intervals for a total t_{SL} of 30 ms and an f_{SL} of 0, 200 and 400 Hz. The mean represents the average of five scans with error bars of ± one standard deviation.

The number of dynamics required for the mapping was investigated by fitting the results from Fig. 4.8 to various number of time dynamics. Tab. 4.5 displays the $R_{1\rho}$ extracted from the signal decay with 2 (0 and 30 ms), 3 (0, 15 and 30 ms), 4 (0, 10, 20 and 30 ms) or 7 (0, 5, 10, 15, 20, 25, 30 ms) time dynamics. Despite slight overestimation of the $R_{1\rho}$ at fewer time dynamics, the results were comparable.

Table 4.5: Extracting $R_{1\rho}$ [Hz] from the signal decay of a reference vial and a vial with 2% 10 μm beads at a varying number of time dynamics to indicate the quality of the fit.

	0% microbeads			**2% microbeads**		
	0 Hz	**200 Hz**	**400 Hz**	**0 Hz**	**200 Hz**	**400 Hz**
2 dyn	15.3	14.9	15.4	15.2	14.5	14.4
3 dyn	16.4	16.0	16.4	16.2	15.5	15.3
4 dyn	16.0	15.8	16.1	15.9	15.2	15.0
7 dyn	14.3	14.0	14.2	14.1	13.3	13.2

The last experiment aimed to investigate the repeatability of the phantom fabrication. A pair containing a reference vial without any beads, and a vial with 1% 20 μm beads was produced five times with 0.30% Gd. They were imaged ten times to obtain a mean and standard deviation of their T_2 values identical to the method used for selecting the susceptibility agent in the system verification (Fig. 4.9).

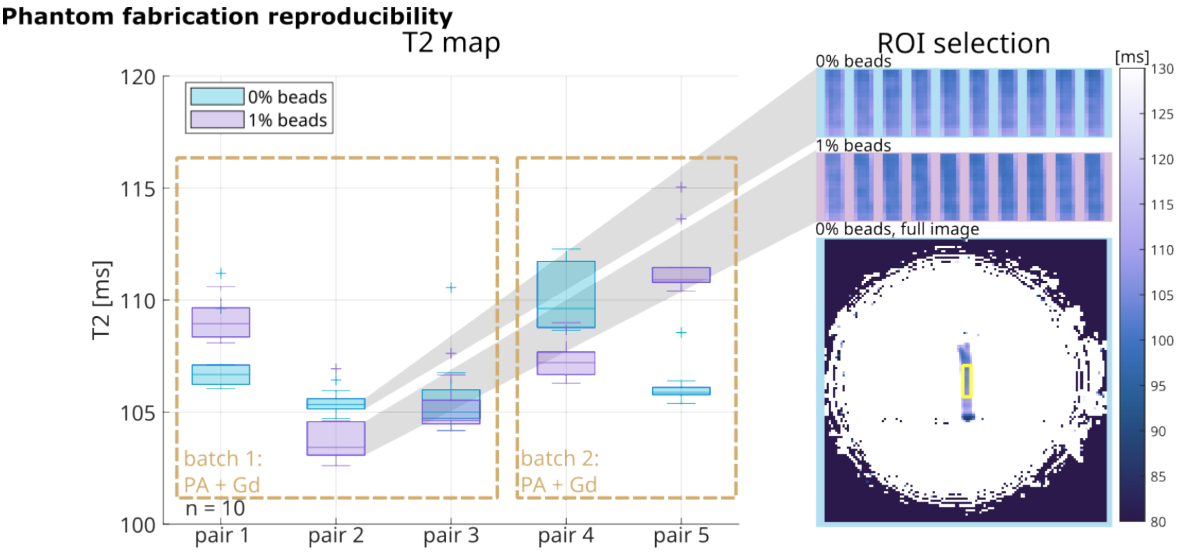

Figure 4.9: Reproducibility of experimental design in presence of a susceptibility agent. 5 identical pairs were produced containing a reference vial and a vial with 1% 20 m microbeads. T_2 results of 10 scans are shown. For the reference and bead-containing vial of pair 2, a zoom in of the ROI is shown for each of the 10 scan repetitions. One full image is displayed below the ROIs, in which the ROI is highlighted with a yellow box.

5

Discussion

This study explored the potential of spin-lock pulse sequences for characterizing microstructures beyond the resolution of conventional MRI. Spatial information was encoded into the signal on a sub-voxel level by hydrogen spins diffusing through intrinsic susceptibility gradients. Simulation experiments demonstrated that the dispersion magnitude and inflection point of the $R_{1\rho}$ dispersion profile provided valuable insights into spatial properties of microstructures. However, phantom experiments did not achieve an optimal experimental configuration. The findings and future research directions will be discussed in two separate sections: simulation and phantom experiments.

5.1. Simulation experiments

The inflection point, marked by the steepest section of the dispersion curve, served as metric for microbead radius estimation (Fig. 4.1). The spin-lock frequency at the inflection point corresponded to the time required for a spin to travel the characteristic length of a perturber [34]. While dispersion magnitude was highly dependent on microstructure concentration and susceptibility differences, the inflection point remained largely independent of these factors. Although the diffusion coefficient affected the inflection point, its variations are limited under physiological conditions. For example, the ADC of gray matter reported in healthy tissue is around $0.9 \cdot 10^{-6} mm^2/ms$, whereas the tissue of patients with dementia has an ADC of approximately $1 \cdot 10^{-6} mm^2/ms$ [46]. The consistent behavior of the inflection point could make it a reliable indicator of microstructure size. However, since the inflection point is a second-order derivative, its quantification is highly sensitive to noise.

Information on microbead radius was provided by the $R_{1\rho}$ dispersion curve within the 2.5-20 μm range (Fig. 4.1A). Within this range, the microbead radius affected both dispersion magnitude and inflection point position. Larger microbeads created less rapidly varying field distortions, thereby shifting the inflection point to a lower spin-lock frequency. However, this effect became negligible for microstructures exceeding 20 μm, and the inflection point stabilized independent of the microbead radius. Beyond 20 μm, the interactional frequency was too low to capture with a spin-lock pulse. Conversely, for beads smaller than 2.5 μm, the field distortions were rapidly varying, averaging the effective magnetic field at all spin-lock frequencies.

Both microstructure concentration and susceptibility shift positively correlated with dispersion magnitude (Fig. 4.1B&C). Higher microbead concentrations enhanced relaxation at low spin-lock frequencies due to increased spatial field variations. Similarly, a larger susceptibility shift resulted in faster relaxation due to stronger field variations surrounding a perturber. In *in vivo* applications, iron deposits are more likely to be detected due to high susceptibility differences rather than high concentrations. Notably, while a clinically relevant range of iron concentration is below 0.02% in the brain, the susceptibility shift of a deposit of four iron atoms is around 10.1 ppm, or equivalent to 8χ in Fig. 4.1C [2].

Relaxation induced by microstructures was highly dependent on the diffusion length. Variations in the diffusion coefficient, D, altered the effective diffusive length, influencing the averaging of field fluctuations (Fig. 4.1D). A lower D reduced field averaging, thereby increasing dispersion magnitude, particularly at low spin-lock frequencies. Below a critical D, the situation approximated the static dephasing regime, where diffusion is negligible, and relaxation becomes reversible with a refocusing pulse. Additionally, diffusion influenced the inflection point, where lower diffusion coefficients shifted the inflection point to lower spin-lock frequencies due to prolonged interactions with field distortions.

It should be noted that the performed simulations considered a singular spherical perturber in a repeating unit cell. At high volume fractions, the effect of multiple spherical perturbers on a hydrogen spin becomes non-negligible, potentially altering relaxation behavior. Furthermore, a random distribution of multiple spherical perturbers may introduce a more complex $R_{1\rho}$ dispersion.

5.2. Phantom experiments

Phantom experiments demonstrated to what extent microstructures could be detected with the current experimental setup. Firstly, phantom fabrication and system identification are discussed, followed by microstructure detection experiments.

The system verification aimed to investigate the effect of the gelling agent and the susceptibility agent. Gelatin, as a common gelling agent, was limited in suitability due to air bubble trapping [41]. Independent degassing cycles with an ultrasonic bath, vacuum pump, and vacuum oven proved to be insufficient for eliminating air bubble formation. Agarose is less sensitive to air bubble trapping; however, high melting temperatures are required, under which conditions polystyrene bead stability cannot be ensured. To mitigate the temperature issue, low-melt agarose was tested for phantom fabrication. Although the reduced melting temperatures preserved bead stability, low-melt agarose did not serve as a suitable agent due to large T_2 reductions, rendering the phantom fabrication highly sensitive to weighing and pipetting errors. Alternatively, polyacrylamide was assessed as gelling agent. Despite the inability of polyacrylamide to reverse gelling for microbead-reuse, it was best suited for the research purpose as it did not lead to air bubble formation, large T_2 reductions, nor high melting temperatures [45].

The spin-diffusion analysis of the effect of the gel matrix indicates that PA had minimal impact on the ADC. From Fig. 4.2B, the diffusion coefficient in PA gel was calculated as $1.94 \cdot 10^{-6}\ mm^2/ms$, which was a reduction of 5.8% from the ADC of the surrounding water. The value reported for water was in agreement with the expected ADC at room temperature [47]. Since the ADC is temperature dependent, lowering the sample temperature could align phantom conditions with clinical values ($1 \cdot 10^{-6} mm^2/ms$) [34]. However, maintaining a stable temperature during MRI acquisition is challenging, as spin-lock sequences deposit energy into the system (typically 1°C [40]) and acquiring a dispersion profile is timely. Refrigerated samples are, therefore, not recommended unless temperature constancy can be ensured.

Regarding the susceptibility agent, holmium (III) chloride hexahydrate induced the largest susceptibility difference from the tested agents. Along with dysprosium ions, holmium possessed the largest effective magnetic moment from the rare earth ions while not greatly reducing dipole-relaxivity [43]. However, the addition of holmium to the medium created an unstable solution where microbeads flocculate (Appendix C). To counter bead aggregations, vials were fabricated with the addition of Triton-X or EDTA, both proving to be suboptimal for providing a stable suspension. Alternatively, the agents $CuSo_4$ and $NiCl_2$ were also unsuited for microstructure detection, respectively due to the prolonged PA gelling time and a color-changing chemical reaction. Therefore, the use of gadolinium as susceptibility agent was investigated. Gd is a well-established contrast agent in MRI that may be used in *in vivo* experiments [48]. Although the maximum concentration was limited by the considerably shortened T_1 and T_2, Gd generated a 30 Hz frequency shift (Tab. 4.2). Hence, gadolinium was selected for further phantom experiments.

The preparatory spin-lock module with adiabatic refocusing pulses was more resilient to B_0 imperfections than the module with block refocusing pulses (Fig. 4.3). In line with previous findings, B_0 insensitivity greatly reduced the banding artifacts in acquired spin-lock images and refocusing adiabatically was a robust method for achieving B_0 insensitivity [40, 49]. The module with adiabatic refocusing was therefore selected for further spin-lock imaging.

Phantom experiments demonstrated minimal changes in the relaxation rate with increasing bead concentrations, suggesting that the current experimental design lacked a considerable effect size. Simulations predicted no measurable f_{SL} dependency on the $R_{1\rho}$ for 3 μm beads, while 10 μm beads should exhibit subtle changes dependent on f_{SL} (Fig. 4.4 & 4.5). However, experimental data showed only a slight increase in relaxation rate with inconsistencies across bead concentrations, which was additionally illustrated in Fig. 4.6. It was hypothesized that variations in Gd concentration were at the root of these inconsistencies. $R_{1\rho}$ is highly dependent on T_2, and slight changes in the gadolinium concentrations altered the T_2 considerably, complicating the detection of the subtle $R_{1\rho}$ variations (2-3 Hz) expected for the current phantom vials.

No clear inflection point was observed in dispersion profiles for 3 and 10 μm beads (Fig. 4.4 and Fig. 4.5). Simulations predicted these results for 3 μm beads, though the dispersion profile for 10 μm beads should be converging to a plateau at 400 Hz. One possible explanation is that the susceptibility gradient was insufficient to induce a measurable change in the relaxation rate. The frequency shift of 0.3% Gd was around 30 Hz, which may not produce sufficient field distortions, which therefore inhibited the identification of an inflection point. In contrast, an *in vivo* deposit of four iron atoms has a susceptibility of 10.1 ppm, equivalent to a $\Delta\Omega$ of 420 Hz [2], and lung alveoli provide a susceptibility difference of 8 ppm within a voxel, equivalent to 336 Hz [50].

The experimental configuration should be optimized to demonstrate microstructure detection *in phantom*. To increase the effect size, a greater magnetic susceptibility difference between the medium and the microstructures must be achieved, possible in one of two ways. Firstly, the configuration can be chosen to allow the use of $HoCl_3 \cdot 6H_20$ as a susceptibility agent to generate a larger frequency shift with minimal reduction in dipole relaxivity. In this regard, adding a high molecular weight PEG coating can increase bead stability in a high ionic strength medium due to steric hindrance (Appendix C). Secondly, gas-filled microbubbles, a well established ultrasound contrast agent, may be used as alternative microstructures [4]. Microbubbles are lipid-shelled circular structures with an air- or gas-filled cavity ranging from 2 to 6 μm with a slightly higher susceptibility shift than polystyrene - 0.36 ppm as compared to 0.1 ppm [30, 43]. Although they are harder to preserve in a stable phantom environment, the simulation results show that larger susceptibility differences are expected to further amplify the observed $T_{1\rho}$ change.

Fig. 4.7 demonstrates negligible signal loss during the SL prepulse in the absence of T_2-shortening Gd. Due to specific absorption rate (SAR) and RF power restrictions, spin-lock magnetization preparations were limited to a short t_{SL}, inhibiting correct mapping of long relaxation times [51]. Increasing the number of shots in multi-shot acquisition could slightly mitigate this limitation by reducing RF power deposition during image readout, providing modestly greater flexibility in prepulse duration [52]. In some cases, the normalized signal exceeded 1 at the end of the prepulse. This likely resulted from insufficient M_z recovery between consecutive scans. The current M_z recovery time of 3000 ms was insufficient for full magnetization regrowth, assuming the T_1 of the medium was around 2400 ms [45]. Although elongating M_z recovery increases signal regrowth, it was impractical for the sequence implemented on our scanner. In our case, unintended RF calibration blocks were introduced by the system into the pulse sequence at longer M_z recovery durations, restricting the prepulse to adhere to the SAR and RF power limit considerably to a maximum f_{SL} of 150 Hz for t_{SL} of 30 ms.

Fig. 4.9 assessed the reproducibility of phantom fabrication for vials with Gd in T_2 maps, resembling a spin-lock pulse sequence of 0 Hz. As gadolinium significantly reduced T2, slight concentration variations affected the results, reducing phantom reproducibility. Fabrication errors outweighed the contribution of the intrinsic susceptibility gradient effect on the relaxation time. Therefore, phantom fabrication with Gd was not reliably reproducible. The use of an alternative susceptibility agent with less effect on the dipole-relaxivity might increase the reproducibility of the phantom.

Regarding the number of time dynamics required to map signal decay, it should be noted that the number of dynamics does not compromise $R_{1\rho}$ quantification. As shown in Fig. 4.8 and Tab. 4.5, the results obtained with a varying number of time dynamics were comparable.

Once a suitable phantom configuration is established, the existing relationship of the spatial frequency to $R_{1\rho}$ should be expanded (Eq. 2.15). The current model assumes a single sinusoidal field variation, which rarely occurs naturally [34]. More complex field variations should be captured for accurate *in vivo* translation.

Finally, a comparative study between $T_{1\rho}$ and T_2 mapping in microstructure detection would assist in the understanding of diffusion through susceptibility gradients. Similar to relating the characteristic perturber frequency to the f_{SL}, the characteristic perturber time is matched to the interval between refocusing pulses. The lower RF power deposition provides added flexibility in the application enabling microstructure detection embedded in tissues with a longer transverse relaxation time. Evaluating the robustness of microstructure detection with both measures would provide valuable insights into the direction that microstructure research should take.

6

Conclusion

Although micrometer-scale structures exist below the resolution of conventional MRI, sub-voxel level information is encoded into the image; the MRI signal is affected by microstructures through the combined influence of susceptibility differences and non-negligible spin diffusion. In this thesis, relaxation under a spin-lock pulse sequence was evaluated for its ability to detect microstructures, characterized as $T_{1\rho}$. A simulation model of a spin-lock pulse sequence showed high sensitivity to microbead radius, concentration, and susceptibility shift through $R_{1\rho}$ dispersion magnitude and inflection point. However, phantom experiments with polystyrene microbeads and gadolinium showed minimal changes in relaxation rate, indicating that signal dynamics were insufficiently influenced by the microstructures, and a stronger susceptibility gradient was required. Additionally, the spin-lock pulse duration was reduced by SAR and RF amplifier limitations, restricting its applications to short relaxation times. By addressing current experimental limitations, spin-lock pulse sequences have the potential to become reliable tools for detecting micrometer-scale structures in the body.

A

Phantom fabrication protocol

An example procedure for fabricating a polyacrylamide gel phantom with polystyrene microbeads is detailed below.

Preparing the medium

To ensure consistency in gel and magnetic properties, microbead samples within one experiment should be produced from the same medium:

1. Pipette the desired amount of polyacrylamide, water, ammonium persulfate and gadolinium into a vial (Tab. A.1).
2. Degas the solution in an ultrasonic bath for at least one minute. Continue until no new air bubbles appear at the surface.
3. Place the solution in an ice bath. Cold temperatures slow down the polymerization process, allowing more time to pipette the solution into the final vials.
4. Pipette the catalyst TEMED into the solution to initialize the polymerization process.

Fabricating the microbead vials

1. Heat a glass beaker with water in the microwave until the temperature reaches 45 °C.
2. Prepare the final vials by labeling the vials and pipetting the required amount of prediluted microbead solution into them.
3. Add the prediluted polyacrylamide solution, while ensuring that the pipet tip is below the surface level to inhibit the introduction of unwanted air into the medium.
4. Place the finished vials in the beaker with warm water to speed up the polymerization process. If the gelling speed is not critical, this is not necessary.

Polyacrylamide gels are stable at room temperature.

Table A.1: Required amounts of polyacrylamide, ammonium persulfate, TEMED, gadolinium Dotarem and Milli-Q for creating a 10 mL batch of prediluted polyacrylamide gel solution.

	Final concentration [%]	**Dilution ratio** **[-]**	**Volume** **[mL]**
40% acrylamide	15.31	2.6	3.830
10 % ammonium persulfate	0.14	71.4	0.140
TEMED	0.14	714	0.014
Gd	1.00	100	0.100
Milli-Q	-	-	5.97

B

Measuring magnetic susceptibility

The frequency shift caused by susceptibility agents was calculated from B_0 maps. The validity of this method was tested by performing the measurements for five vials with known $\Delta\Omega$ and $\Delta\chi$ and comparing the outcomes. The vials contained an increasing concentration of holmium (III) chloride hexahydrate. The $\Delta\Omega$ and $\Delta\chi$ values were compared to previously reported values, where $[Ho]$ is the concentration of holmium in mM [43]:

$$\Delta\chi = -9.03 \cdot 10^{-6} + 0.566 \cdot 10^{-6} \cdot [Ho]. \tag{B.1}$$

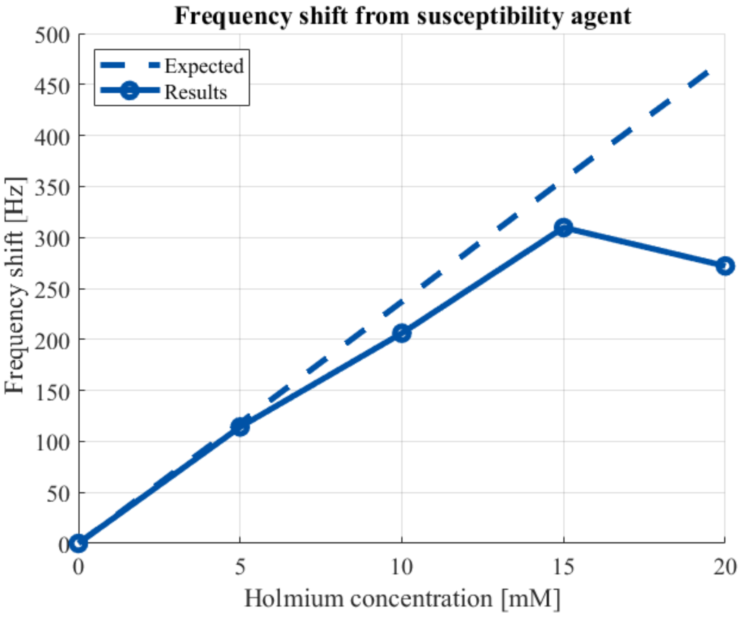

Figure B.1: A susceptibility agent was added to alter the frequency shift of the medium. To confirm the method of calculating the frequency shift, a range of holmium concentrations was imaged and compared to the expected frequency shifts reported in literature.

Fig. B.1 visualizes the measured and expected relationship between the holmium concentration and $\Delta\Omega$. Especially at lower holmium concentrations, there was a close match between the measured and expected $\Delta\Omega$. The underestimation at frequency shifts > 300 Hz may be attributed to the short dTE of 1 ms affecting the quality of the linear fit. In a B_0 map, the frequency shift is fit to the phase data consisting of linear and periodic components. At high $\Delta\Omega$, phase decoherence might have progressed beyond the point of being accurately identified, causing an underestimation of the $\Delta\Omega$. The $\Delta\Omega$ alongside the $\Delta\chi$ are summarized in Tab. B.1.

Table B.1: Vials used to confirm the validity of the method of measuring the susceptibility difference. The expected $\Delta\chi$ and $\Delta\Omega$ of the susceptibility agent holmium (III) chloride hexahydrate served as reference values to which results from the susceptibility experiments were compared [43].

Vial	**Medium**	**Holmium [mM]**	**Expected $\Delta\chi$ [ppm]**	**Measured $\Delta\chi$ [ppm]**	**Expected $\Delta\Omega$ [Hz]**	**Measured $\Delta\Omega$ [Hz]**
1-ref	9% PA	0	0	0	0	0
2	9% PA	5	2.77	2.68	118	114
3	9% PA	10	5.57	4.84	237	206
4	9% PA	15	8.38	7.26	357	309
5	9% PA	20	11.15	6.39	475	272

C

DLVO theory

The addition of holmium (III) chloride hexahydrate to a polystyrene microbead solution in a PA gel caused microbead aggregations. This behavior can be explained by the theory of colloidal stability developed by Derjaguin, Landau, Vervey and Overbeek (DLVO) [53]. The DLVO theory states that the primary reason for aggregation is the balance between attractive van der Waals forces and repulsive electrostatic forces.

Van der Waals forces arise from interactions from the induced dipoles of molecules. Electrostatic repulsion depends on electric double layer (EDL) interactions of charged substrates; a charged particle is surrounded by a layer of counterions which exerts a repulsive force when identical particles approach. The length of the EDL, termed the Debye length, determines the strength of the repulsive force. A longer EDL inhibits particles from aggregating due to the high force required to overcome the repulsive force. The balance between these two forces determines the DLVO profile, as illustrated in Fig. C.1 (left, green).

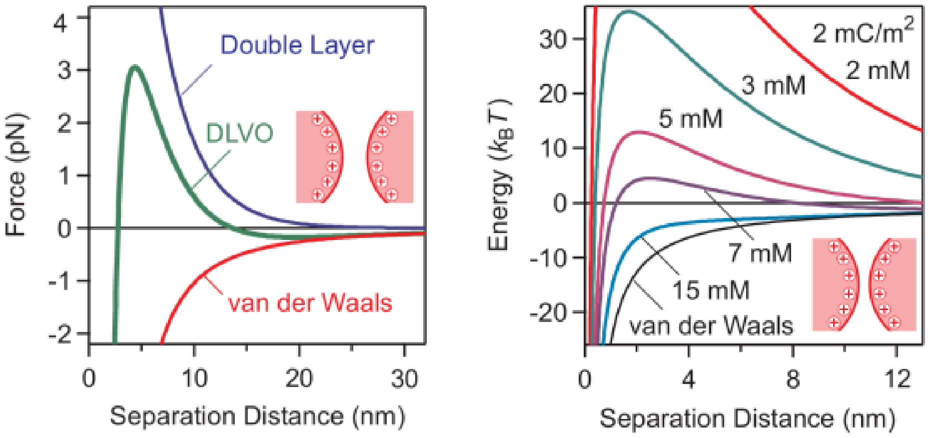

Figure C.1: The left figure displays the force profile of the interaction between two identical particles as described by the DLVO theory. The total DLVO curve is compared to the van der Waals attraction force and the EDL repulsion force. The right graph displays the DLVO curve for a range of salt concentrations, where high salt levels demonstrate dominant attractive van der Waals forces. Figure adapted from [53].

The strength of electrostatic repulsion depends on the salt concentration of the solution. An increase in salt concentration progressively decreases the exerted repulsive forces, as displayed in Fig.C.1 (right). From a certain salt concentration onward, the attractive forces dominate.

The reduction in electrostatic repulsion due to an increased salt concentration arises from the shortening of the EDL. The EDL is highly dependent on the ionic strength of the medium, where an increase in ionic strength leads to a reduction in Debye length. The ionic strength of the solution is given by:

$$I = \frac{1}{2}\sum_i z_i^2 c_i, \tag{C.1}$$

where I is the ionic strength expressed in mol/L, z the valence of an ion of type i and c the ion concentration in mol/L. The contributions from all ion types i in a solution are summed. As salts increase the ionic strength and thereby decrease the Debye length, the DLVO profile becomes more attractive.

Whether the DLVO profile is attractive or repulsive determines the behavior of the particles in a solution (Fig. C.2). In solutions that exhibit a repulsive profile, particles repel and a stable suspension forms. When the DLVO profile is attractive, identical particles approach until contact, where they remain due to van der Waals attraction. Over time, larger aggregations form that will eventually sediment. The latter is referred to as an unstable suspension.

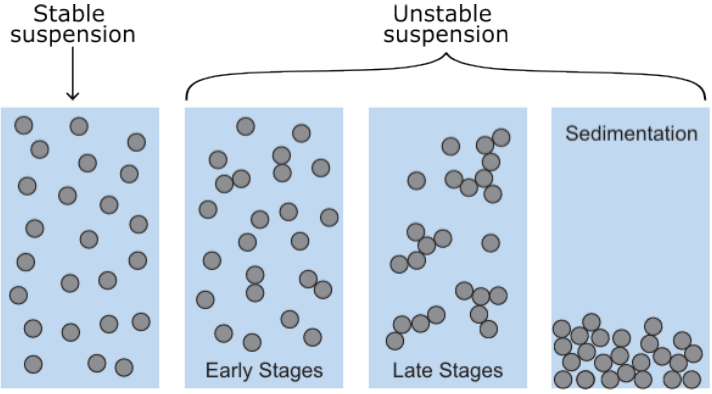

Figure C.2: When the DLVO profile is strongly repulsive, identical particles will repel and form a stable suspension. When the profile is attractive, the particles approach until contact. Bead aggregations will form that increase in size over time. Figure adapted from [53].

Holmium chloride hexahydrate

In the presence of holmium (III) chloride hexahydrate, NH_2-coated polystyrene microbeads formed aggregations when gelled in polyacrylamide. The observed behavior may be explained by applying the DLVO theorem. Holmium is a trivalent ion, which induced a stark increase in ionic strength according to Eq. C.1, shifting the DLVO profile from repulsive to attractive. The resultant suspension was unstable, forming progressively larger bead aggregations over time and eventually leading to sedimentation.

Bibliography

[1] George Bartzokis et al. “Brain ferritin iron may influence age-and gender-related risks of neurodegeneration”. In: *Neurobiology of aging* 28.3 (2007), pp. 414–423.

[2] Stefan Ropele and Christian Langkammer. “Iron quantification with susceptibility”. In: *NMR in Biomedicine* 30.4 (2017), e3534.

[3] Lukas R Buschle et al. “Diffusion-mediated dephasing in the dipole field around a single spherical magnetic object”. In: *Magnetic Resonance Imaging* 33.9 (2015), pp. 1126–1145.

[4] Richard P Kennan, Jianhui Zhong, and John C Gore. “Intravascular susceptibility contrast mechanisms in tissues”. In: *Magnetic resonance in medicine* 31.1 (1994), pp. 9–21.

[5] Jennifer MJ Richards et al. “In vivo mononuclear cell tracking using superparamagnetic particles of iron oxide: feasibility and safety in humans”. In: *Circulation: Cardiovascular Imaging* 5.4 (2012), pp. 509–517.

[6] S Majumdar and JC Gore. “Studies of diffusion in random fields produced by variations in susceptibility”. In: *Journal of Magnetic Resonance (1969)* 78.1 (1988), pp. 41–55.

[7] Jerrold L Boxerman et al. “MR contrast due to intravascular magnetic susceptibility perturbations”. In: *Magnetic resonance in medicine* 34.4 (1995), pp. 555–566.

[8] Robert Weisskoff et al. “Microscopic susceptibility variation and transverse relaxation: theory and experiment”. In: *Magnetic Resonance in Medicine* 31.6 (1994), pp. 601–610.

[9] Frank Q Ye and Peter S Allen. “Relaxation enhancement of the transverse magnetization of water protons in paramagnetic suspensions of red blood cells”. In: *Magnetic resonance in medicine* 34.5 (1995), pp. 713–720.

[10] Ulrich Karl Laemmli. “Cleavage of structural proteins during the assembly of the head of bacteriophage T4”. In: *nature* 227.5259 (1970), pp. 680–685.

[11] Anwar R Padhani et al. “Imaging oxygenation of human tumours”. In: *European radiology* 17 (2007), pp. 861–872.

[12] Irene Tropres et al. “Vessel size imaging”. In: *Magnetic Resonance in Medicine: An Official Journal of the International Society for Magnetic Resonance in Medicine* 45.3 (2001), pp. 397–408.

[13] Fatemeh Adelnia et al. “Tissue characterization using R1rho dispersion imaging at low locking fields”. In: *Magnetic Resonance Imaging* 84 (2021), pp. 1–11.

[14] Irtiza Ali Gilani and Raimo Sepponen. “Quantitative rotating frame relaxometry methods in MRI”. In: *NMR in Biomedicine* 29.6 (2016), pp. 841–861.

[15] Jared Guthrie Cobb, Jingping Xie, and John C Gore. “Contributions of chemical and diffusive exchange to T1ρ dispersion”. In: *Magnetic resonance in medicine* 69.5 (2013), pp. 1357–1366.

[16] Alfred G Redfield. “Nuclear magnetic resonance saturation and rotary saturation in solids”. In: *Physical Review* 98.6 (1955), p. 1787.

[17] S Chopra, RED McClung, and RB Jordan. “Rotating-frame relaxation rates of solvent molecules in solutions of paramagnetic ions undergoing solvent exchange”. In: *Journal of Magnetic Resonance (1969)* 59.3 (1984), pp. 361–372.

[18] DG Davis, ME Perlman, and RE London. “Direct measurements of the dissociation-rate constant for inhibitor-enzyme complexes via the T1ρ and T2 (CPMG) methods”. In: *Journal of Magnetic Resonance, Series B* 104.3 (1994), pp. 266–275.

[19] E Lammentausta et al. “T2, Carr–Purcell T2 and T1ρ of fat and water as surrogate markers of trabecular bone structure”. In: *Physics in Medicine & Biology* 53.3 (2008), p. 543.

[20] Zhongliang Zu, Vaibhav Janve, and John C Gore. “Spin-lock imaging of intrinsic susceptibility gradients in tumors”. In: *Magnetic resonance in medicine* 83.5 (2020), pp. 1587–1595.

[21] Robert W Brown et al. *Magnetic resonance imaging: physical principles and sequence design*. John Wiley & Sons, 2014.

[22] Rosalind Sadleir and Atul Singh Minhas. *Electrical Properties of Tissues: Quantitative Magnetic Resonance Mapping*. Vol. 1380. Springer Nature, 2022.

[23] Joao Tourais, Chiara Coletti, and Sebastian Weingärtner. "Brief Introduction to MRI Physics". In: *Advances in Magnetic Resonance Technology and Applications*. Vol. 7. Elsevier, 2022, pp. 3–36.

[24] Joseph Larmor. "LXIII. On the theory of the magnetic influence on spectra; and on the radiation from moving ions". In: *The London, Edinburgh, and Dublin Philosophical Magazine and Journal of Science* 44.271 (1897), pp. 503–512.

[25] ML Lauzon. "A Beginner's Guide to Bloch Equation Simulations of Magnetic Resonance Imaging Sequences". In: *arXiv preprint arXiv:2009.02789* (2020).

[26] Jing Yuan et al. "Quantification of T1ρ relaxation by using rotary echo spin-lock pulses in the presence of B0 inhomogeneity". In: *Physics in Medicine & Biology* 57.15 (2012), p. 5003.

[27] John T Spear and John C Gore. "Effects of diffusion in magnetically inhomogeneous media on rotating frame spin–lattice relaxation". In: *Journal of Magnetic Resonance* 249 (2014), pp. 80–87.

[28] Felix T Kurz et al. "Generalized moment analysis of magnetic field correlations for accumulations of spherical and cylindrical magnetic perturbers". In: *Frontiers in Physics* 4 (2016), p. 46.

[29] Dmitriy A Yablonskiy and E Mark Haacke. "Theory of NMR signal behavior in magnetically inhomogeneous tissues: the static dephasing regime". In: *Magnetic resonance in medicine* 32.6 (1994), pp. 749–763.

[30] Felix T Kurz et al. "Theoretical model of the single spin-echo relaxation time for spherical magnetic perturbers". In: *Magnetic resonance in medicine* 71.5 (2014), pp. 1888–1895.

[31] Lukas Reinhold Buschle et al. "Vessel radius mapping in an extended model of transverse relaxation". In: *Magnetic Resonance Materials in Physics, Biology and Medicine* 31 (2018), pp. 531–551.

[32] Lukas R Buschle et al. "Spin dephasing around randomly distributed vessels". In: *Journal of Magnetic Resonance* 299 (2019), pp. 12–20.

[33] CH Ziener et al. "Spin echoes: full numerical solution and breakdown of approximative solutions". In: *Journal of Physics: Condensed Matter* 31.15 (2019), p. 155101.

[34] John T Spear, Zhongliang Zu, and John C Gore. "Dispersion of relaxation rates in the rotating frame under the action of spin-locking pulses and diffusion in inhomogeneous magnetic fields". In: *Magnetic resonance in medicine* 71.5 (2014), pp. 1906–1911.

[35] Suraj D Serai. "Basics of magnetic resonance imaging and quantitative parameters T1, T2, T2*, T1rho and diffusion-weighted imaging". In: *Pediatric radiology* 52.2 (2022), pp. 217–227.

[36] Sridhar R Charagundla et al. "Artifacts in T1ρ-weighted imaging: correction with a self-compensating spin-locking pulse". In: *Journal of Magnetic Resonance* 162.1 (2003), pp. 113–121.

[37] Xiaojuan Li et al. "In vivo T1ρ mapping in cartilage using 3D magnetization-prepared angle-modulated partitioned k-space spoiled gradient echo snapshots (3D MAPSS)". In: *Magnetic Resonance in Medicine: An Official Journal of the International Society for Magnetic Resonance in Medicine* 59.2 (2008), pp. 298–307.

[38] Aurelien Bustin et al. "Magnetic resonance myocardial T1ρ mapping: Technical overview, challenges, emerging developments, and clinical applications". In: *Journal of Cardiovascular Magnetic Resonance* 25.1 (2023), p. 34.

[39] Maximilian Gram et al. "Balanced spin-lock preparation for B1-insensitive and B0-insensitive quantification of the rotating frame relaxation time T1ρ". In: *Magnetic Resonance in Medicine* 85.5 (2021), pp. 2771–2780.

[40] Walter RT Witschey II et al. "Artifacts in T1ρ-weighted imaging: Compensation for B1 and B0 field imperfections". In: *Journal of magnetic resonance* 186.1 (2007), pp. 75–85.

[41] Pippa Storey and Dmitry S Novikov. "Signatures of microstructure in gradient-echo and spin-echo signals". In: *Magnetic Resonance in Medicine* 92.1 (2024), pp. 269–288.

[42] Arvind P Pathak, B Douglas Ward, and Kathleen M Schmainda. “A novel technique for modeling susceptibility-based contrast mechanisms for arbitrary microvascular geometries: the finite perturber method”. In: *Neuroimage* 40.3 (2008), pp. 1130–1143.

[43] Chris JG Bakker and Remmert de Roos. “Concerning the preparation and use of substances with a magnetic susceptibility equal to the magnetic susceptibility of air”. In: *Magnetic Resonance in Medicine: An Official Journal of the International Society for Magnetic Resonance in Medicine* 56.5 (2006), pp. 1107–1113.

[44] Soumaya Sridi et al. “Improved myocardial scar visualization with fast free-breathing motion-compensated black-blood T1-rho-prepared late gadolinium enhancement MRI”. In: *Diagnostic and interventional imaging* 103.12 (2022), pp. 607–617.

[45] T Boursianis et al. “MRI diffusion phantoms: ADC and relaxometric measurement comparisons between polyacrylamide and agarose gels”. In: *European Journal of Radiology* 139 (2021), p. 109696.

[46] H Takahashi et al. “Clinical application of apparent diffusion coefficient mapping in voxel-based morphometry in the diagnosis of Alzheimer’s disease”. In: *Clinical radiology* 72.2 (2017), pp. 108–115.

[47] Jui H Wang. “Self-diffusion coefficients of water”. In: *The Journal of Physical Chemistry* 69.12 (1965), pp. 4412–4412.

[48] Hee-Kyung Kim, Gang Ho Lee, and Yongmin Chang. “Gadolinium as an MRI contrast agent”. In: *Future Medicinal Chemistry* 10.6 (2018), pp. 639–661.

[49] Michael Garwood and Lance DelaBarre. “The return of the frequency sweep: designing adiabatic pulses for contemporary NMR”. In: *Journal of magnetic resonance* 153.2 (2001), pp. 155–177.

[50] Robert Mulkern et al. “Lung parenchymal signal intensity in MRI: a technical review with educational aspirations regarding reversible versus irreversible transverse relaxation effects in common pulse sequences”. In: *Concepts in Magnetic Resonance Part A* 43.2 (2014), pp. 29–53.

[51] Chiara Coletti et al. “Robust cardiac T 1 ρ T _ 1_ ρ mapping at 3T using adiabatic spin-lock preparations”. In: *Magnetic resonance in medicine* 90.4 (2023), pp. 1363–1379.

[52] Robin M Heidemann et al. “Perspectives and limitations of parallel MR imaging at high field strengths”. In: *Neuroimaging Clinics* 16.2 (2006), pp. 311–320.

[53] Gregor Trefalt and Michal Borkovec. “Overview of DLVO theory”. In: *Laboratory of Colloid and Surface Chemistry, University of Geneva, Switzerland* 304 (2014).